minerals

MDPI

Article

Geochemical and Geostatistical Analysis of Manganese Mineralization in the Kulu Area (Central Anatolia, Konya, Türkiye)

Bilgehan Yabgu Horasan

Department of Environmental Protection Technologies, Sarayönü Vocational School, Selçuk University, Konya 42430, Türkiye; bilgehanyabgu@gmail.com

Abstract

Manganese is a raw material of increasing strategic importance owing not only to its fundamental role in steel production but also to its use in battery technologies, chemical processes, environmental applications, and advanced industrial fields. With the ongoing energy transition, the growing demand for battery-grade manganese has made it increasingly important to reassess the geological, mineralogical, and geochemical characteristics of manganese occurrences that are known from limited data. In this study, the manganese mineralization observed in the Kulu–Kozanlı area of Central Anatolia was investigated using field observations, ore microscopy, XRD, SEM–EDS, major oxide and trace element geochemistry, and spatial data based on sampling locations. Major oxide and trace element data indicate that manganese enrichment is not homogeneous and is concentrated in specific zones. The results of Spearman correlation, PCA, HCA, and factor analysis reveal a clear opposition between MnO and SiO_2, whereas MnO tends to increase together with Cu, Ba, V, Ga, and Sr. XRD, SEM–EDS, and ore microscopy findings show that the mineralization is mainly represented by a Mn oxide/oxyhydroxide assemblage composed of manganite and pyrolusite, with local braunite. When all findings are evaluated together, the Kulu manganese mineralization is interpreted as a lithologically heterogeneous Mn mineralization associated with radiolarite/chert and carbonate–cherty levels within the Dereköy ophiolitic mélange and consistent with hydrothermal influence.

Keywords: radiolarian chert; Mn oxides; trace-element geochemistry; hydrothermal influence; ophiolitic mélange

Check for updates

Academic Editor: Liqiang Yang

Received: 11 June 2026
Revised: 9 July 2026
Accepted: 22 July 2026
Published: 26 July 2026

Copyright: © 2026 by the author. Licensee MDPI, Basel, Switzerland. This article is an open access article distributed under the terms and conditions of the Creative Commons Attribution (CC BY) license.

1. Introduction

Manganese is one of the essential alloying elements that improves mechanical strength, hardness, and metallurgical performance, particularly in steel production. In addition, manganese and its compounds are used in different fields, including the chemical industry, construction materials, electronics, environmental technologies, agriculture, and battery technologies. In recent years, the increasing demand for manganese in high-technology sectors associated with the energy transition has led to this element being considered not only as a traditional metallurgical raw material but also as a strategic resource. High-purity manganese compounds, such as electrolytic manganese dioxide and manganese sulfate monohydrate, have become important components for cathode materials in lithium-ion batteries [1–6]. This shift in demand increases the importance of manganese for the global energy transition and advanced manufacturing technologies [7–9]. Re-examination of

the geological, mineralogical, and geochemical characteristics of manganese occurrences that were previously known from limited data or had not been investigated in detail has therefore gained importance [10,11].

In the investigation of mineral deposits, evaluating field observations together with geological/geophysical data is important for delimiting mineralized areas and determining exploration targets [12]. Manganese mineralizations may vary in terms of origin and formation mechanisms because they can develop in different geological settings. In the literature, manganese oxide/oxyhydroxide deposits can be classified as hydrogenetic, diagenetic, and hydrothermal deposits according to their mineralogical properties, chemical compositions, and tectonic settings [13–15]. Manganese deposits observed in Türkiye are evaluated under different groups according to the geological units in which they occur, their ages, host-rock characteristics, and chemical, mineralogical, and structural characters. These include deposits hosted in sedimentary successions belonging to the Paleotethys, Karakaya, and Neotethys; occurrences associated with Mesozoic carbonate successions in the Western Taurides; mineralizations related to the Black Sea volcanic arc belt; and manganese deposits within the Tertiary sediments of the Thrace Basin [16]. Mn oxide occurrences associated with radiolarian cherts have also been reported within the İzmir–Ankara–Erzincan Suture Zone and related ophiolitic mélange units [17,18]. In the evaluation of the Mn mineralization in the Kulu area, lithological position, host–rock relationship, ore mineralogy, and major oxide–trace element geochemistry were therefore assessed.

The Mn mineralization in the Kulu area is observed as surface mineralizations associated with radiolarite/chert, siliceous/radiolaritic levels, and locally carbonate–cherty levels within the Dereköy ophiolitic mélange [19,20]. This geological position makes it necessary to evaluate the mineralization not only in terms of Mn enrichment but also in terms of lithological relationship, ore mineralogy, and trace element behavior. The Kulu manganese mineralization was investigated using field observations, ore microscopy, XRD, SEM–EDS, and major oxide–trace element geochemistry. The aim of the study is to determine the lithological units with which the mineralization is associated, the mineralogical and geochemical character of the manganiferous zones, the relationship between Mn enrichment and the siliceous/radiolaritic component and trace elements, and the clues provided by the available data regarding the formation of the mineralization.

2. Geological Setting

2.1. Regional Geological Framework

The basement rocks of the Tuz Gölü Basin are represented by the Kütahya–Bolkardağı Metamorphites in the western and southwestern parts of the basin, whereas accretionary-prism-type units form the basement in the northern and northwestern parts [21–24] (Figure 1).

The basement rocks exposed in the western and southwestern parts of the basin were defined as the Kütahya–Bolkardağı Metamorphites (KBM) by [25]. The KBM consists of rocks deposited in a platform setting during the Paleozoic–Mesozoic interval [23,24].

The basement units in the northern and northwestern parts of the basin are represented by the Central Anatolian Ophiolitic Complex according to [26]. These units developed during the closure of the İzmir–Ankara–Erzincan Ocean and were thrust southward over the Kütahya–Bolkardağı Metamorphites as an accretionary-prism-type assemblage [27].

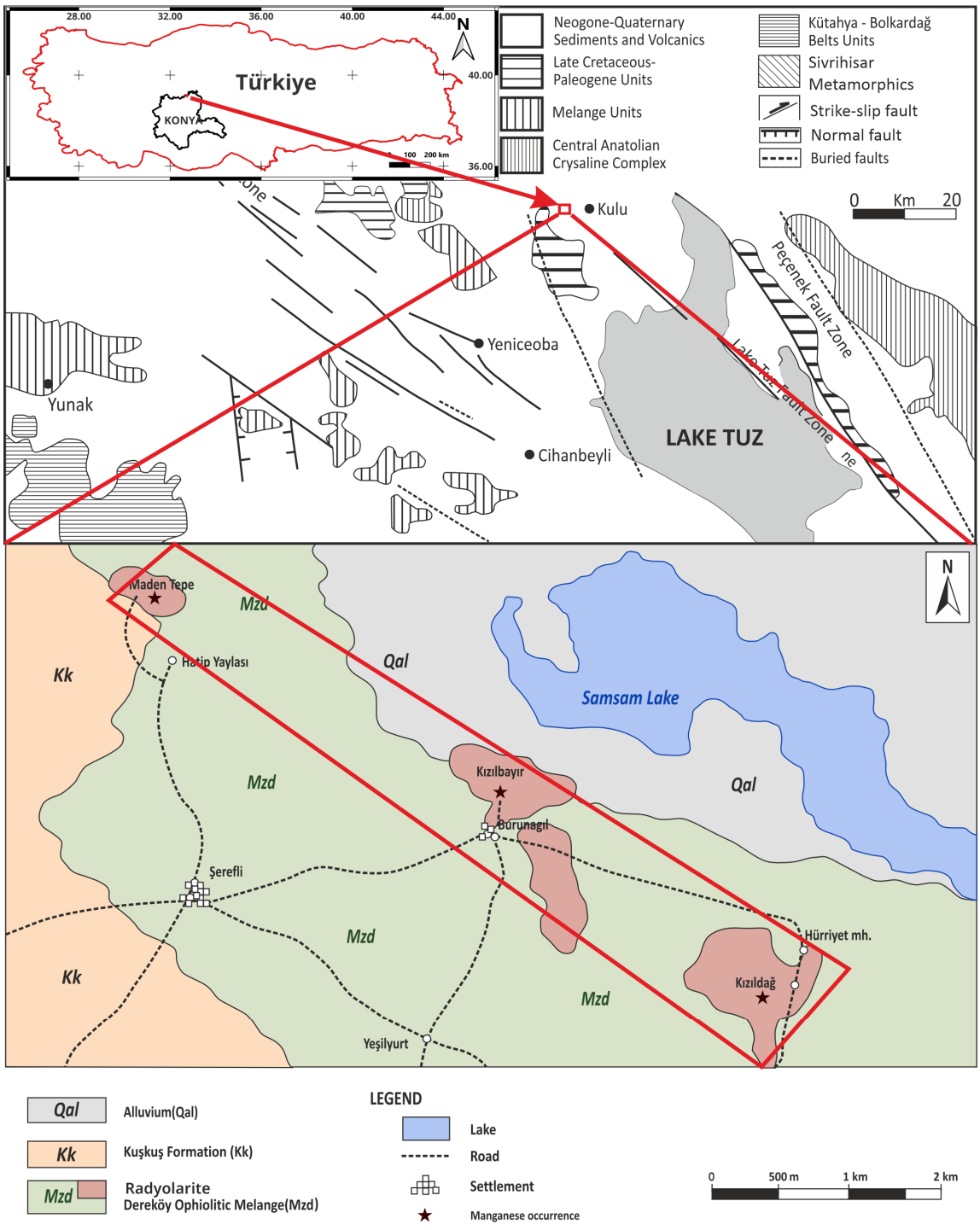


Figure 1. Location of the study area and its regional geological setting. The figure shows the location of the study area within Türkiye, the regional geological and structural framework of the Tuz Gölü area, and the geological map of the Kulu area, highlighting the spatial relationships of the Kızıldağ, Burunağıl, and Madentepe manganese mineralization areas with the Dereköy ophiolitic mélange, Kuşkuş Formation, and alluvial units. The red line delineates the boundary of the study area [23,27–29].

2.2. Geology of the Kulu–Kozanlı Area

The main units exposed in the study area consist of the Dereköy ophiolitic mélange, the Kuşkuş Formation, and recent alluvial deposits. These units represent both the basement

rock assemblages related to the oceanic closure process and the Upper Cretaceous–Tertiary cover units of the region.

The most important unit in terms of manganese mineralization in the study area is the Dereköy ophiolitic mélange. This unit forms a complex tectonic assemblage composed of ophiolitic, volcanic, carbonate, and siliceous blocks of different ages and origins (Figure 1).

2.2.1. Dereköy Ophiolitic Mélange (Mzd)

This unit, which consists of undifferentiated slices and blocks of mafic, ultramafic, volcanic, ophiolitic, and sedimentary rocks, was named the Dereköy ophiolitic mélange by [19]. In Ref. [29], the unit was described as the Ankara mélange. The unit represents one of the important records of the regional tectonic evolution in the study area and reflects the ophiolitic–accretionary-prism character associated with the closure of the İzmir–Ankara–Erzincan Ocean.

The Dereköy ophiolitic mélange includes green, white, purple, and variegated gabbro, diabase, serpentinite, spilitic pillow lava, andesite, basalt, tuff, agglomerate, and marble, as well as Triassic neritic and pelagic limestone blocks. In addition, slices and blocks composed of pink, grey, brown, and red claystone, siltstone, sandstone, clayey limestone, shale, and volcanic rocks, locally containing radiolarite interbeds, are also observed within the unit [19,20].

In the study area, the Dereköy ophiolitic mélange contains diabase, serpentinite, locally mafic rock products, and blocks with different ages and lithological characteristics. The main blocks within the mélange consist of Jurassic–Cretaceous radiolarite–chert blocks, Jurassic–Cretaceous limestone blocks, and Permian limestone blocks [19,20]. The Permian limestone blocks are thought to have probably been derived from Permian limestone olistoliths within the Karakaya Formation. The Jurassic–Cretaceous limestone blocks, on the other hand, have been suggested to be derived from the Bilecik Limestone [30].

2.2.2. Kuşkuş Formation (Kk)

The Kuşkuş Formation was first defined by [29] as a unit deposited during the Santonian–Campanian interval and composed of red mudstone, marl, and clayey limestone. The formation is considered one of the lowermost units of the succession formed by the Haymana Basin rocks.

The literature indicates that the Kuşkuş Formation has limited outcrops east of Haymana and around Cingirli village. The unit unconformably overlies rocks of the Sakarya Zone and shows a conformable and transitional relationship with the overlying Haymana Formation. The dominant lithology of the formation consists of reddish-brown mudstone, sandstone, marl, and clayey limestone [31].

The Kuşkuş Formation was deposited under terrestrial and shallow-marine environmental conditions. In most studies, it is regarded as equivalent to the red mudstone, marl, and clayey limestone levels that are commonly shown as undifferentiated within the lowermost parts of the Haymana Formation. With these characteristics, the unit represents the Upper Cretaceous transitional-environment deposits of the region [20].

2.2.3. Alluvium (Qal)

Older units in the study area are locally covered by recent alluvial deposits. The alluvial deposits are generally observed along valley floors, stream beds, and low-topography areas. These units consist of loosely consolidated recent clastic materials of gravel, sand, silt, and clay size.

The alluvial deposits represent the youngest units in the study area. Although they are not considered to be directly related to mineralization, they are important in terms of surface weathering, transportation, and cover processes [28].

3. Materials and Methods

The study area is located within the boundaries of Kulu district, approximately 170 km north of Konya city center. The study covers the manganese mineralizations observed in the Kızıldağ, Burunağıl, and Madentepe areas, which are located within a general investigation area of approximately 100 km^2. The manganese occurrences examined in this study are represented by mineralized zones exposed over an area of approximately 20 km^2 within these three areas. During the field studies, the geological and lithological characteristics of the region were observed, and the locations where manganese mineralization occurs, host–rock relationships, mineralization style, color, texture, fracture–crack relationships, and field relationships with siliceous/carbonate components were investigated. Sampling was carried out to represent the manganese-bearing zones observed in the field, the associated lithological units, and the variations in mineralization; in this context, 41 manganese-bearing rock samples were collected from the Kızıldağ, Burunağıl, and Madentepe areas. The samples were collected from outcrops containing visible Mn mineralization and from zones associated with siliceous/radiolaritic, carbonate-cherty, and ophiolitic mélange-related units accompanying these outcrops.

The collected manganese-bearing rock samples were crushed, ground, and homogenized under laboratory conditions. The samples prepared for geochemical analysis were powdered and packed as approximately 40–50 g sample packages. Major oxide analyses were performed for SiO_2, Al_2O_3, Fe_2O_3, CaO, MgO, Na_2O, K_2O, Cr_2O_3, TiO_2, MnO, and P_2O_5, whereas trace element and selected REE analyses were carried out for Cu, Ba, V, Co, Ni, Zn, Ga, As, Sr, Mo, Sn, Sb, Pb, Sm, Eu, Gd, Dy, Ho, and Er. Geochemical analyses were performed at the METU MERLAB Chemical Analysis Laboratory. Prior to analysis, the samples were digested in a microwave digestion system using an aqua regia + HF mixture, and boric acid was used after digestion to remove residual HF. Analytical quality control was ensured using USGS AGV-2 and OREAS 60d certified reference materials, and the reproducibility of the measurements was controlled to be %RSD < 3.

SEM–EDS investigations of selected samples were carried out using a Zeiss EVO LS20 scanning electron microscope, Carl Zeiss AG, Oberkochen, Germany, and point chemical compositions were analyzed using a Bruker EDS detector, Bruker Nano GmbH, Berlin, Germany. The energy resolution of the EDS detector is approximately 123 eV. For the identification of mineral phases, the samples were reduced to a grain size of 100–200 μm, and XRD analyses were performed using a Bruker D8 Advance X-ray diffractometer, Bruker AXS GmbH, Karlsruhe, Germany. SEM–EDS and XRD analyses were conducted at the Advanced Technology Research and Application Center of Selçuk University (İLTEK).

Selected manganese-bearing samples from the study area were prepared as polished sections for ore microscopy investigations. The polished sections were prepared at the Department of Geological Engineering, Konya Technical University, and the examinations were also conducted in the same department. The cut sample surfaces were first prepared on a horizontal lap machine using SiC abrasives and then progressively abraded with 220, 400, 600, and 800 grit SiC papers. Final polishing was completed on a felt disc using 9, 3, and 1 μm diamond pastes, respectively. The polished samples were examined under reflected light using a polarizing microscope, and the textural characteristics, fracture–crack relationships, filling styles, and mineral paragenesis of the manganese minerals were evaluated.

Within the scope of multivariate evaluations, Hierarchical Cluster Analysis (HCA) and Principal Component Analysis (PCA) were performed using SPSS v26 software. These analyses were used to determine the geochemical similarities and differences among sample groups and to more clearly evaluate the distinction between mineralization and host-rock/lithological components. Before PCA and HCA, the variables were standardized

using Z-score standardization. This procedure was applied because the dataset includes major oxides expressed in weight percent (wt.%) and trace elements and rare earth elements expressed in ppm. Thus, variables measured in different units and scales were made comparable within the same multivariate analysis. In HCA, similarity relationships among samples and variables were evaluated based on Euclidean distance, and clusters were generated using Ward's linkage method. In PCA, a correlation matrix based on standardized variables was used; the principal components were interpreted by considering eigenvalues greater than 1, the cumulative explained variance, and the general trend of the scree plot. Therefore, PCA and HCA results were evaluated not as direct genetic evidence, but as explanatory statistical tools supporting geochemical trends, sample groups, and the distinction between ore and host-rock components [32–34]. The sample locations and spatial distributions of selected geochemical parameters were visualized using QGIS software (v3.44.11). During the preparation of this manuscript, generative AI tools were used only for English language editing and reference formatting. All AI-assisted outputs were reviewed, corrected and approved by the authors. Generative AI tools were not used for geochemical data analysis, statistical calculations or scientific interpretation.

4. Results

4.1. Field Observations and Lithological Characteristics

The Mn-bearing levels in the study area are macroscopically observed as dark grey to blackish-brown zones, locally showing rusty weathering surfaces (Figure 2a,c,d). In samples associated with radiolarite/chert, the Mn-bearing parts occur together with siliceous and thin-bedded cherty-radiolaritic rocks, locally as banded, lenticular, and irregular masses (Figure 2a,c,f). In these samples, the Mn-bearing zones are mostly developed within the siliceous host rock and display a relationship with bedding and fracture systems (Figure 2a,e).

In areas where carbonate levels and radiolaritic/cherty units show transitional relationships, manganese occurrences are observed particularly within radiolaritic/cherty levels, where they occur as lenticular, irregular, and locally fracture-filling forms. The coexistence of light-colored carbonate components and dark-colored cherty-radiolaritic levels allows these lithological transitions to be distinguished macroscopically in the field (Figure 2b,d). In altered zones, reddish-brown weathering colors, loose/clastic textures, and locally grey-black Mn-bearing material are distinctive features (Figure 2e). Field observations indicate that the Kulu manganese mineralization developed not as a single uniform ore body, but as Mn-bearing zones associated with different lithological components (Figure 2a–f).

The 41 rock samples collected from the field represent the Mn-bearing zones identified during macroscopic observations and the associated siliceous/radiolaritic, cherty, carbonate-cherty, and altered lithological components. Sampling was carried out in a targeted manner, considering Mn-bearing levels, Mn oxide-bearing zones, siliceous/radiolaritic units, carbonate-cherty Mn-bearing levels, and altered zones (Table 1). Samples S1–S8, S11–S14, and S17–S26 generally represent Mn-bearing radiolaritic/cherty zones and Mn-bearing siliceous/radiolaritic components. Samples S9, S10, S15, and S16 represent low-MnO siliceous/radiolaritic zones; S27 represents a Mn-bearing siliceous/radiolaritic-cherty zone; S28–S32 represent carbonate-cherty Mn-bearing levels; S35 represents a carbonate-cherty Mn-bearing zone; and S40 represents a carbonate-cherty Mn-bearing transition zone. Samples S33–S34 represent altered radiolaritic/cherty zones, S36, S37, and S39 represent radiolaritic altered zones, S38 represents an altered mixed lithological zone, and S41 represents a siliceous/radiolaritic zone. Therefore, the geochemical results were interpreted by considering that the samples do not represent a single homogeneous ore lithology, but rather different lithological/field components.

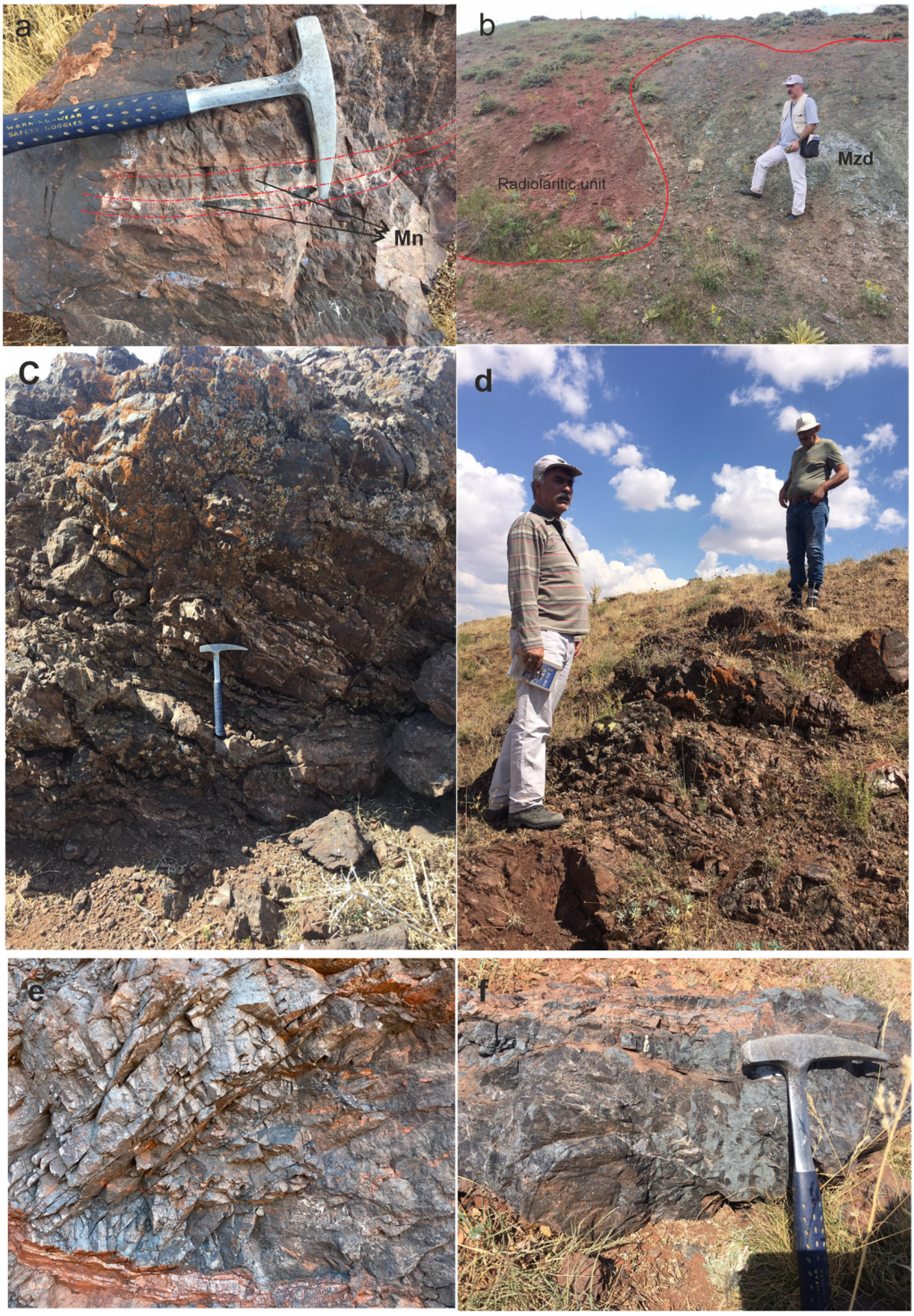


Figure 2. Field photographs of the Kulu manganese mineralization. (**a**) Dark-colored Mn-bearing vein/filling zones developed within siliceous radiolaritic/cherty rocks. (**b**) Field relationship between the radiolaritic unit and the Dereköy ophiolitic mélange in the Burunağıl area. (**c**) Macroscopic appearance of Mn-bearing zones associated with radiolaritic/cherty rocks. (**d**) Mn-bearing outcrop observed within the ophiolitic mélange or along radiolaritic/cherty levels associated with the mélange. (**e**) Fracture-controlled and locally altered Mn-bearing zone within radiolaritic/cherty rocks. (**f**) Mn-bearing block/lenticular mass associated with siliceous radiolaritic/cherty rocks. Field photographs were taken by the author during the field studies.

Table 1. Location information, field/lithological descriptions, and MnO values of the Kulu manganese samples.

Sample No.	Sampling Area	Easting	Northing	Lithological/Field Description	MnO (%)
S1	Kızıldağ	478,309	4,325,191	Mn-bearing radiolaritic/cherty zone	30.08
S2	Kızıldağ	478,257	4,325,112	Mn-bearing radiolaritic/cherty zone	40.54
S3	Kızıldağ	478,240	4,325,036	Mn-bearing radiolaritic/cherty zone	30.21
S4	Kızıldağ	478,417	4,325,082	Mn-bearing radiolaritic/cherty zone	43.13
S5	Kızıldağ	478,334	4,324,996	Mn-bearing radiolaritic/cherty zone	47.39
S6	Kızıldağ	478,438	4,324,978	Mn-bearing siliceous/radiolaritic zone	15.88
S7	Kızıldağ	478,485	4,325,010	Mn-bearing siliceous/radiolaritic zone	23.63
S8	Kızıldağ	478,556	4,325,028	Mn-bearing radiolaritic/cherty zone	32.02
S9	Kızıldağ	478,509	4,324,665	Siliceous/radiolaritic zone	3.40
S10	Kızıldağ	478,473	4,324,562	Siliceous/radiolaritic zone	3.40
S11	Kızıldağ	478,437	4,324,486	Mn-bearing siliceous/radiolaritic zone	23.89
S12	Kızıldağ	478,293	4,324,453	Mn-bearing siliceous/radiolaritic zone	21.18
S13	Kızıldağ	478,156	4,324,469	Mn-bearing radiolaritic/cherty zone	30.21
S14	Kızıldağ	478,175	4,324,498	Mn-bearing siliceous/radiolaritic zone	18.21
S15	Kızıldağ	478,222	4,324,508	Siliceous/radiolaritic zone	5.27
S16	Kızıldağ	478,222	4,324,879	Siliceous/radiolaritic zone	7.15
S17	Kızıldağ	478,240	4,324,940	Mn oxide-bearing radiolaritic/cherty zone	64.56
S18	Kızıldağ	478,162	4,325,014	Mn oxide-bearing radiolaritic/cherty zone	52.94
S19	Kızıldağ	478,331	4,325,135	Mn oxide-bearing radiolaritic/cherty zone	52.94
S20	Kızıldağ	478,207	4,324,738	Mn oxide-bearing radiolaritic/cherty zone	61.98
S21	Kızıldağ	478,155	4,324,729	Mn-bearing siliceous/radiolaritic zone	15.24
S22	Kızıldağ	478,091	4,324,734	Mn-bearing siliceous/radiolaritic zone	26.73
S23	Kızıldağ	478,136	4,324,643	Mn-bearing siliceous/radiolaritic zone	13.82
S24	Kızıldağ	478,197	4,324,614	Mn-bearing radiolaritic/cherty zone	32.54
S25	Kızıldağ	478,243	4,324,635	Mn-bearing siliceous/radiolaritic zone	23.63
S26	Kızıldağ	478,423	4,324,994	Mn oxide-bearing radiolaritic/cherty zone	65.85
S27	Burunağıl	477,250	4,325,865	Mn-bearing siliceous/radiolaritic-cherty zone	40.41
S28	Burunağıl	476,232	4,325,905	Carbonate-cherty Mn-bearing horizon	32.02
S29	Burunağıl	476,263	4,325,938	Carbonate-cherty Mn-bearing horizon	56.81
S30	Burunağıl	476,303	4,325,960	Carbonate-cherty Mn-bearing horizon	37.06
S31	Burunağıl	476,090	4,325,788	Carbonate-cherty Mn-bearing horizon	58.10
S32	Madentepe	476,114	4,325,830	Carbonate-cherty Mn-bearing horizon	36.41
S33	Madentepe	476,822	4,326,596	Altered radiolaritic/cherty zone	0.67
S34	Madentepe	476,731	4,326,728	Altered radiolaritic/cherty zone	0.76
S35	Madentepe	472,445	4,330,622	Carbonate-cherty Mn-bearing zone	32.67
S36	Madentepe	472,511	4,330,581	Radiolaritic altered zone	0.28
S37	Burunağıl	472,511	4,330,489	Radiolaritic altered zone	0.26
S38	Burunağıl	472,426	4,330,498	Altered mixed lithological zone	0.40
S39	Madentepe	472,386	4,330,542	Radiolaritic altered zone	0.97
S40	Madentepe	472,750	4,330,317	Carbonate-cherty Mn-bearing transition zone	24.15
S41	Burunağıl	472,805	4,330,223	Siliceous/radiolaritic zone	1.21

4.2. Ore Mineralogy and Textural Characteristics

In the polished sections prepared from samples collected during the field study, Mn oxide/oxyhydroxide phases are observed as dark grey to black, relatively high-reflectance phases occurring mostly as fillings along fracture–crack lines, irregular aggregates, and locally disseminated zones. In some samples, the Mn-bearing phases are concentrated along narrow fracture fillings, whereas in others they show a more irregular and void-filling character. These textural features indicate that the Mn oxide/oxyhydroxide phases developed as fillings along fracture–crack lines and voids (Figure 3).

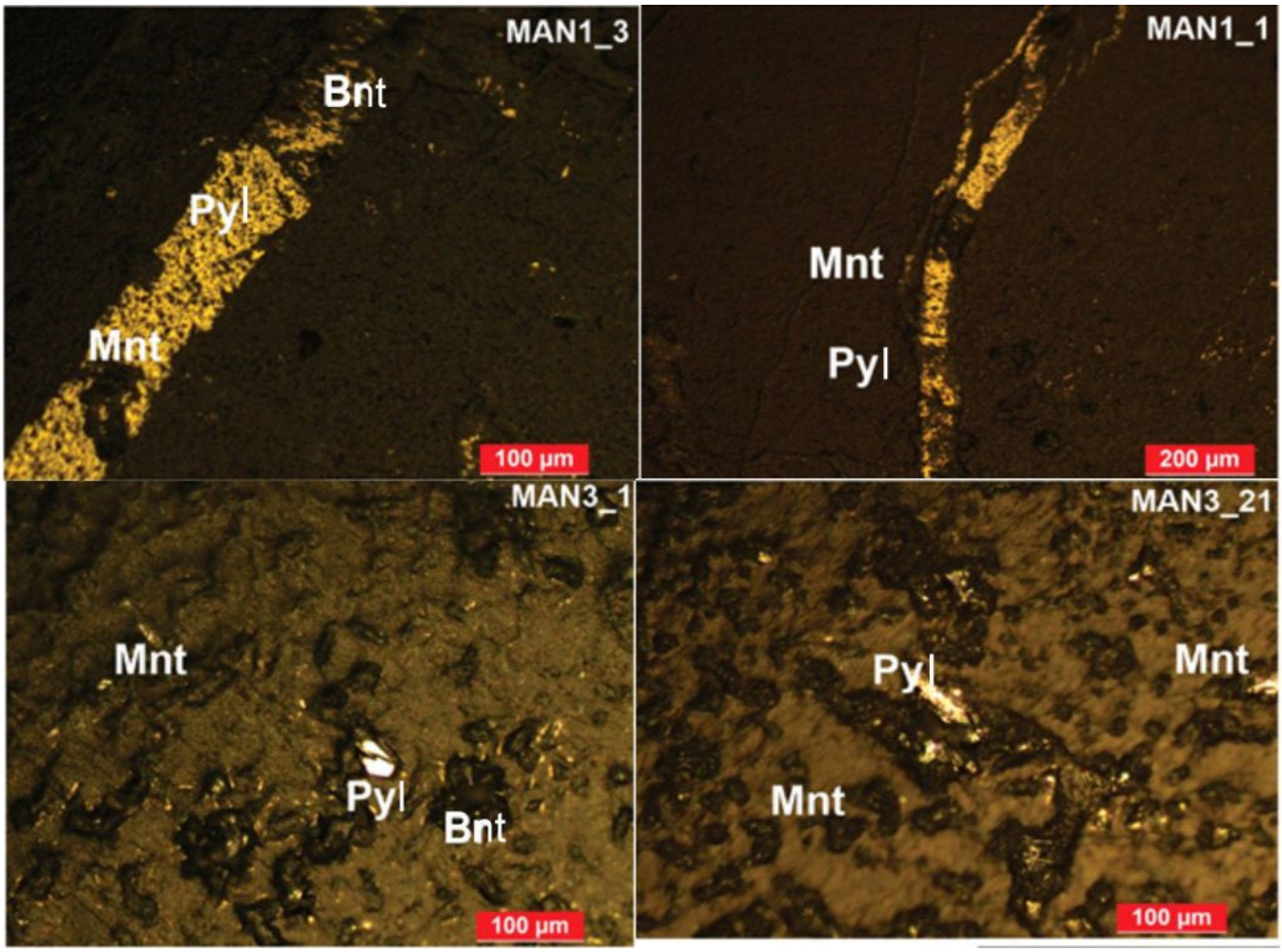


Figure 3. Reflected-light photomicrographs of manganese ore samples from the study area showing manganite (Mnt), pyrolusite (Pyl), and braunite (Bnt).

In the XRD patterns, manganite (Mnt) and pyrolusite (Pyl) peaks are clearly observed. Braunite (Bnt) peaks are also distinguished; however, they occur as a lower-intensity accompanying Mn phase compared with manganite and pyrolusite. The presence of quartz (Qz) peaks in all patterns supports the association of the Mn-bearing levels with siliceous/radiolaritic-cherty components. Calcite (Cal) peaks were not identified in all patterns but were distinguished only in some samples. This indicates that carbonate gangue is not dominant throughout the samples, but locally accompanies the Mn-bearing levels (Figure 4).

In the SEM image, the Mn-rich phase exhibits fine platy/rod-like crystal aggregates and an aggregate texture (Figure 5a).

The unnormalized total of the EDS analysis (Figure 5b) given in Table 2 is 87.57%. This low total is related to the fact that the analyzed point was not taken from an ideal, single-phase, flat mineral surface, but rather from a rough Mn oxide/oxyhydroxide aggregate composed of fine platy/rod-like crystals, as also observed in the SEM image.

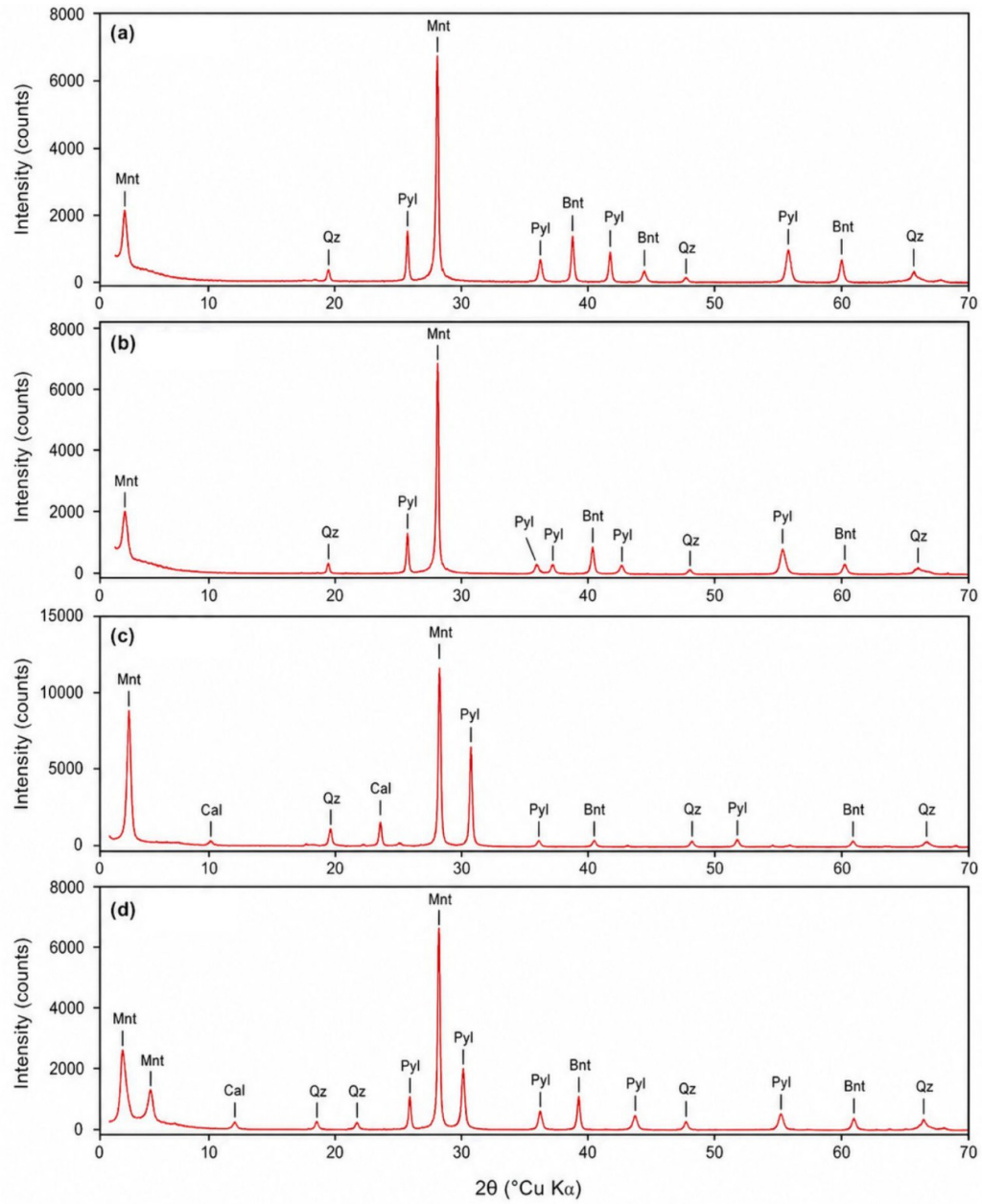


Figure 4. XRD patterns of manganese ore samples from the study area: (**a**) manganite (Mnt), pyrolusite (Pyl), braunite (Bnt), and quartz (Qz); (**b**) manganite (Mnt), pyrolusite (Pyl), braunite (Bnt), and quartz (Qz); (**c**) manganite (Mnt), pyrolusite (Pyl), braunite (Bnt), quartz (Qz), and calcite (Cal); (**d**) manganite (Mnt), pyrolusite (Pyl), braunite (Bnt), quartz (Qz), and calcite (Cal).

Table 2. Quantitative EDS composition of the analyzed Mn-rich phase.

Element	Series	Unnormalized wt.%	Normalized wt.%	Atomic %	Error %
Manganese	K-series	51.48	58.79	29.27	1.4
Oxygen	K-series	34.34	39.21	67.03	4.1
Carbon	K-series	1.23	1.41	3.21	0.3
Silicon	K-series	0.28	0.32	0.31	0.0
Calcium	K-series	0.24	0.27	0.19	0.0
Total		87.57	100.00	100.00	

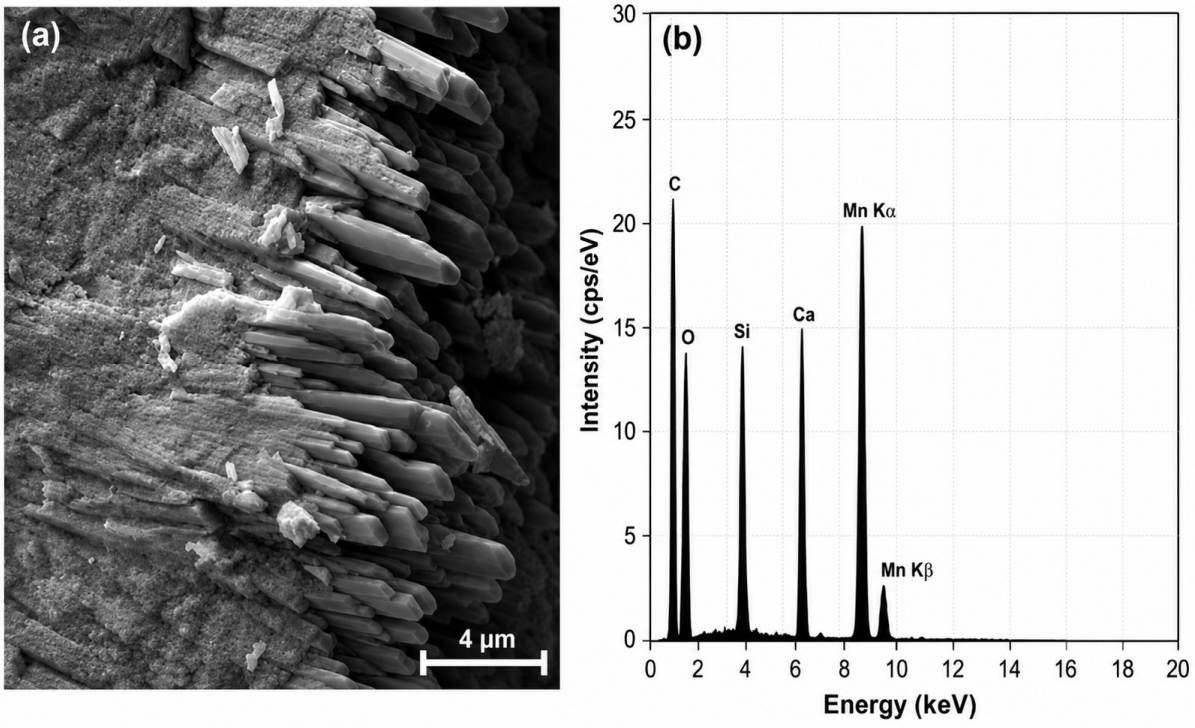


Figure 5. SEM image (**a**) and EDS analytical spectrum (**b**) of the Mn-rich phase.

The fact that Mn oxide minerals commonly occur as fine-grained, poorly crystalline, chemically variable, and finely intergrown phases requires careful interpretation of phase identifications made by SEM–EDS [35,36].

4.3. Geochemical Characteristics of Mn-Bearing Samples

Samples collected from the field were classified, based on the field/lithological descriptions given in Table 1, as Mn-bearing radiolaritic/cherty zones, Mn-bearing siliceous/radiolaritic zones, carbonate-cherty Mn-bearing levels, altered radiolaritic/cherty zones, and siliceous/radiolaritic components. Major oxide and trace element data were therefore evaluated by considering that the samples do not represent a single homogeneous lithology, but rather different field/lithological components (Table 1).

The major oxide contents of the Mn-bearing samples from the study area show a wide range of variation. SiO_2 contents range from 28.88 to 94.55%, Al_2O_3 from 0.40 to 3.16%, Fe_2O_3 from 0.17 to 25.73%, CaO from 0.06 to 19.45%, MgO from 0.03 to 4.49%, Na_2O from 0.04 to 0.19%, K_2O from 0.04 to 2.18%, Cr_2O_3 from 0.00 to 0.46%, TiO_2 from 0.01 to 0.16%, MnO from 0.26 to 65.85%, and P_2O_5 from 0.02 to 0.92% (Table 3).

The wide variation in SiO_2, MnO, Fe_2O_3, and CaO values among the samples indicates marked geochemical heterogeneity within the dataset. The high SiO_2 values reflect the contribution of radiolaritic host rock or siliceous gangue components to the geochemical composition of the samples. The wide concentration range of MnO indicates that manganese enrichment developed at variable intensities among the samples. Variations in Fe_2O_3, MgO, and Cr_2O_3 may be related to the contribution of mafic–ultramafic rocks within the ophiolitic mélange or to alteration effects in altered lithological components. The increase in CaO values in some samples suggests the local involvement of carbonate gangue or carbonate host-rock components in the system.

Table 3. Major oxide compositions of the Kulu Mn-bearing samples (wt.%).

Sample	SiO_2	Al_2O_3	Fe_2O_3	CaO	MgO	Na_2O	K_2O	Cr_2O_3	TiO_2	MnO	P_2O_5
S1	64.39	0.94	0.70	0.19	0.18	0.18	0.15	0.05	0.03	30.08	0.46
S2	55.41	0.81	0.76	0.17	0.15	0.19	0.11	0.03	0.03	40.54	0.69
S3	66.53	0.93	1.00	0.15	0.17	0.17	0.14	0.04	0.03	30.21	0.23
S4	53.69	0.79	0.67	0.17	0.15	0.19	0.11	0.03	0.03	43.13	0.69
S5	48.77	0.89	1.22	0.18	0.18	0.17	0.13	0.03	0.03	47.39	0.23
S6	83.21	0.62	0.71	0.18	0.05	0.17	0.06	0.05	0.02	15.88	0.02
S7	73.80	0.72	0.77	0.43	0.06	0.18	0.12	0.04	0.03	23.63	0.23
S8	64.39	0.77	0.71	0.49	0.09	0.16	0.13	0.03	0.03	32.02	0.23
S9	92.41	0.43	0.93	0.07	0.03	0.16	0.08	0.09	0.02	3.40	0.92
S10	94.55	0.51	1.04	0.06	0.04	0.17	0.09	0.11	0.02	3.40	0.69
S11	73.37	0.47	0.59	0.17	0.08	0.13	0.07	0.05	0.01	23.89	0.46
S12	75.51	0.40	1.27	0.08	0.03	0.13	0.05	0.00	0.01	21.18	0.69
S13	63.75	0.47	0.66	0.16	0.04	0.13	0.06	0.00	0.01	30.21	0.23
S14	77.65	0.47	0.50	0.08	0.06	0.14	0.06	0.04	0.01	18.21	0.69
S15	91.56	0.45	0.64	0.12	0.04	0.12	0.08	0.05	0.02	5.27	0.23
S16	88.99	0.49	0.86	0.09	0.03	0.12	0.08	0.00	0.02	7.15	0.23
S17	32.73	1.15	0.43	0.14	0.33	0.10	0.19	0.02	0.03	64.56	0.23
S18	41.29	1.44	0.47	0.14	0.43	0.11	0.25	0.01	0.04	52.94	0.23
S19	44.50	1.23	0.57	0.15	0.35	0.10	0.22	0.03	0.04	52.94	0.11
S20	35.94	0.77	0.76	0.16	0.09	0.11	0.09	0.03	0.03	61.98	0.46
S21	78.94	0.83	0.83	0.10	0.07	0.16	0.13	0.05	0.03	15.24	0.23
S22	69.10	0.91	1.06	0.19	0.11	0.14	0.14	0.08	0.04	26.73	0.02
S23	82.57	0.87	1.07	0.12	0.08	0.15	0.24	0.09	0.04	13.82	0.02
S24	65.25	0.77	0.83	0.17	0.09	0.13	0.12	0.06	0.03	32.54	0.11
S25	74.02	0.81	0.84	0.36	0.14	0.14	0.12	0.06	0.03	23.63	0.46
S26	28.88	1.97	1.60	0.24	0.30	0.04	0.34	0.01	0.16	65.85	0.39
S27	54.76	0.68	1.60	0.19	0.09	0.15	2.18	0.00	0.03	40.41	0.34
S28	43.43	1.25	0.17	19.45	2.14	0.05	0.16	0.00	0.01	32.02	0.62
S29	31.66	1.06	0.17	5.90	2.45	0.04	0.31	0.01	0.01	56.81	0.48
S30	45.14	1.08	2.03	13.57	2.11	0.04	0.36	0.00	0.02	37.06	0.50
S31	32.30	0.94	1.36	4.45	1.36	0.05	0.33	0.01	0.02	58.10	0.46
S32	43.85	1.08	0.39	15.11	2.64	0.04	0.06	0.01	0.02	36.41	0.53
S33	63.75	3.16	25.73	1.14	4.49	0.08	1.07	0.34	0.05	0.67	0.16
S34	66.74	2.97	23.45	1.01	3.67	0.09	0.93	0.46	0.02	0.76	0.14
S35	46.85	1.11	0.31	16.93	2.95	0.05	0.04	0.00	0.01	32.67	0.53
S36	85.78	2.06	4.90	3.11	3.43	0.08	0.35	0.08	0.06	0.28	0.69
S37	86.00	2.02	4.79	2.50	3.18	0.08	0.37	0.06	0.06	0.26	0.57
S38	85.14	1.98	4.50	3.16	3.40	0.11	0.34	0.05	0.05	0.40	0.76
S39	83.86	2.10	4.53	3.32	3.13	0.08	0.43	0.03	0.07	0.97	0.46
S40	67.60	1.06	1.52	4.27	0.33	0.13	1.52	0.08	0.08	24.15	0.23
S41	91.56	0.85	1.73	2.66	0.48	0.10	0.20	0.10	0.03	1.21	0.46
Min	28.88	0.40	0.17	0.06	0.03	0.04	0.04	0.00	0.01	0.26	0.02
Max	94.55	3.16	25.73	19.45	4.49	0.19	2.18	0.46	0.16	65.85	0.92
Mean	64.62	1.08	2.41	2.47	0.96	0.12	0.29	0.06	0.03	27.02	0.39
S. Dv.	19.48	0.65	5.23	4.87	1.35	0.05	0.42	0.09	0.03	20.09	0.23

Trace element contents also show marked variability (Table 4). Cu ranges from 29 to 2500 ppm, Ba from 1 to 5300 ppm, V from 1 to 438 ppm, Co from 0.2 to 197 ppm, Ni from 30 to 566 ppm, Zn from 25 to 282 ppm, Ga from 3 to 144 ppm, As from 4 to 223 ppm, Sr from 0.2 to 619 ppm, Mo from 1 to 186 ppm, Sn from 0.13 to 181 ppm, Sb from 0.49 to 48 ppm, and Pb from 0.7 to 796 ppm.

Table 4. Trace element and selected REE compositions of the Kulu Mn-bearing samples (ppm).

SN	Cu	Ba	V	Co	Ni	Zn	Ga	As	Sr	Mo	Sn	Sb	Pb	Sm	Eu	Gd	Dy	Ho	Er
S1	1600	550	252	45	79	105	22	27	181	106	0.46	19	13.1	0.88	1.26	0.83	0.74	0.16	0.49
S2	2200	730	324	59	103	125	54	34	231	143	0.4	28	15.2	0.73	0.24	0.66	0.58	0.12	0.39
S3	1800	590	264	48	85	85	51	28	191	127	0.4	23	13.7	0.81	0.25	0.73	0.68	0.14	0.42
S4	2500	780	334	64	119	116	59	36	261	165	0.34	31	15.1	0.67	0.24	0.55	0.54	0.12	0.38
S5	2300	1020	363	79	144	139	59	36	268	154	0.67	32	70	1.25	0.39	1.06	0.96	0.19	0.57
S6	141	480	79	29	43	27	30	10	90	23	0.4	1.8	17.6	0.4	0.14	0.31	0.27	0.06	0.18
S7	235	570	122	39	57	42	38	11	145	35	0.64	2.5	15.7	0.58	0.19	0.44	0.4	0.08	0.28
S8	389	700	166	51	78	95	43	18	178	50	0.39	5.2	24	0.69	0.23	0.54	0.52	0.1	0.34
S9	82	250	36	18	36	43	9	4	35	14	0.98	1.1	8.5	0.38	0.11	0.28	0.23	0.04	0.13
S10	100	230	34	15	30	30	9	4	34	8	0.47	1.4	9.1	0.58	0.15	0.46	0.34	0.06	0.18
S11	249	540	158	53	95	75	36	29	144	85	0.51	9.8	0.9	0.67	0.22	0.57	0.71	0.15	0.47
S12	135	420	146	32	90	80	35	27	111	86	0.71	6.6	0.7	0.51	0.16	0.45	0.56	0.12	0.4
S13	257	570	164	48	92	79	43	27	131	101	1.39	6.1	1	0.7	0.23	0.62	0.76	0.15	0.5
S14	132	440	112	29	60	54	31	21	92	75	0.43	4.4	0.7	0.52	0.17	0.43	0.56	0.11	0.38
S15	38	320	34	28	33	36	11	4	45	18	0.32	0.9	1.2	0.93	0.15	0.4	0.36	0.07	0.21
S16	29	300	44	42	33	47	14	9	50	25	0.37	0.7	1.2	0.45	0.14	0.4	0.36	0.07	0.22
S17	2400	4030	345	197	334	282	83	28	286	64	0.36	40	796	5.7	1.6	4.9	0.2	0.07	0.2
S18	2000	4120	317	189	296	230	84	27	272	62	0.44	26	745	4.9	1.5	4.1	0.19	0.07	0.21
S19	1700	5300	316	176	253	226	81	29	288	71	1.09	20	719	4.6	1.5	3.8	0.18	0.07	0.22
S20	1410	860	419	114	188	142	94	43	249	186	0.5	15	16.1	1.16	0.35	0.99	0.8	0.17	0.52
S21	530	430	135	37	55	30	32	9	85	48	0.29	7.5	17.8	0.78	0.19	0.75	0.52	0.11	0.33
S22	830	490	208	70	95	83	52	17	120	54	0.4	9.5	12.8	0.84	0.21	0.77	0.58	0.12	0.4
S23	420	390	116	38	60	60	31	8	82	25	0.36	6.1	21	0.78	0.19	0.77	0.53	0.11	0.3
S24	1150	620	252	66	106	102	65	26	165	106	0.55	14	16.1	0.8	0.22	0.8	0.65	0.14	0.42
S25	1020	600	211	92	92	87	51	21	165	81	0.37	13	16.6	0.78	0.22	0.81	0.55	0.12	0.37
S26	750	1070	432	99	108	93	144	45	239	20	0.72	4.4	95	10.8	2.2	14.9	5.7	1	2.7
S27	451	2	438	147	83	80	20	65	0.2	50	0.13	4.2	5.3	4.5	2.3	1.72	0.2	0.07	0.1
S28	810	1500	106	10	272	63	70	12	356	5	0.23	0.91	1.9	2.1	0.66	1.79	1.79	0.36	1.11
S29	1790	2600	193	12	453	128	124	14	612	14	0.15	1.9	2.4	2.9	0.89	2.3	2.4	0.49	1.48
S30	1020	2080	166	25	320	99	89	14	448	7	0.4	1.1	3.6	2.7	0.83	2.4	2.4	0.5	1.52
S31	1830	2290	225	45	383	86	101	11	619	16	0.25	2.8	3.4	2.9	1.1	2.6	2.6	0.54	1.65
S32	540	1790	120	59	350	106	96	21	430	10	0.17	2	5.6	4	1.2	3.6	3.7	0.78	2.4
S33	48	6	1	52	566	75	24	223	12	9	181	48	123	8.1	2	9.4	8.3	1.6	4.5
S34	105	5	1	54	505	55	19	188	1	5	151	43	101	6.2	1.5	7	6.5	1.24	3.6
S35	600	1480	98	0.2	353	70	79	18	404	3.9	0.15	0.89	2.2	3.6	1.1	3.3	3.6	0.76	2.4
S36	164	45	66	34	189	134	4	8	60	4.3	0.56	0.87	10.6	3.4	0.81	3.7	3.1	0.56	1.6
S37	157	40	70	32	187	137	4	8	57	1	0.7	0.88	12.7	3.6	0.85	3.9	3.2	0.6	1.62
S38	160	77	72	33	201	106	5	7	69	6.2	0.6	0.93	8.9	3.4	0.81	3.7	3	0.55	1.53
S39	171	300	75	35	202	138	5	7	101	1.1	0.87	0.91	10.9	4	0.95	4.2	3.4	0.63	1.8
S40	278	1	355	104	73	94	43	16	0.2	28	0.18	1.6	7	4.7	2.1	2.7	0.2	0.07	0.2
S41	52	70	20	10	47	25	3	6	50	1	0.48	0.49	11	2.3	0.51	2.5	1.9	0.36	1.1
Min	29	1	1	0.2	30	25	3	4	0.2	1	0.13	0.49	0.7	0.38	0.11	0.28	0.18	0.04	0.1
Max	2500	5300	438	197	566	282	144	223	619	186	181	48	796	10.8	2.3	14.9	8.3	1.6	4.5
Mean	794.46	943.56	180.22	58.76	169.46	95.34	47.49	29.17	179.45	51.06	8.56	10.72	72.5	2.45	0.73	2.34	1.58	0.31	0.92
S. Dv.	786.21	1196.45	126.82	47.29	140.44	54.73	35.08	42.66	155.49	50.86	36.25	13.09	195.83	2.36	0.66	2.83	1.88	0.35	1.01

These broad ranges indicate that trace element enrichment in the Mn-bearing zones is not homogeneous and that distinct local geochemical variations occur among the samples. In particular, it has been experimentally shown that elements such as Co, Ni, and Zn can be retained by co-precipitation or adsorption with Mn oxides [37]. The high adsorption and trace element retention capacity of Mn oxide/oxyhydroxide minerals may influence the distribution of heavy metals and certain trace elements in natural systems [35].

4.4. Spatial Variation in Geochemical Indicators Based on Sample Points

MnO, SiO_2, CaO, Fe_2O_3, Ba, Cu, V, and Al_2O_3 values are shown by graduated symbols at the sample locations (Figure 6). These maps were used to evaluate the sample points where manganese enrichment is concentrated and their relationships with siliceous/radiolaritic, carbonate-cherty, or altered lithological components.

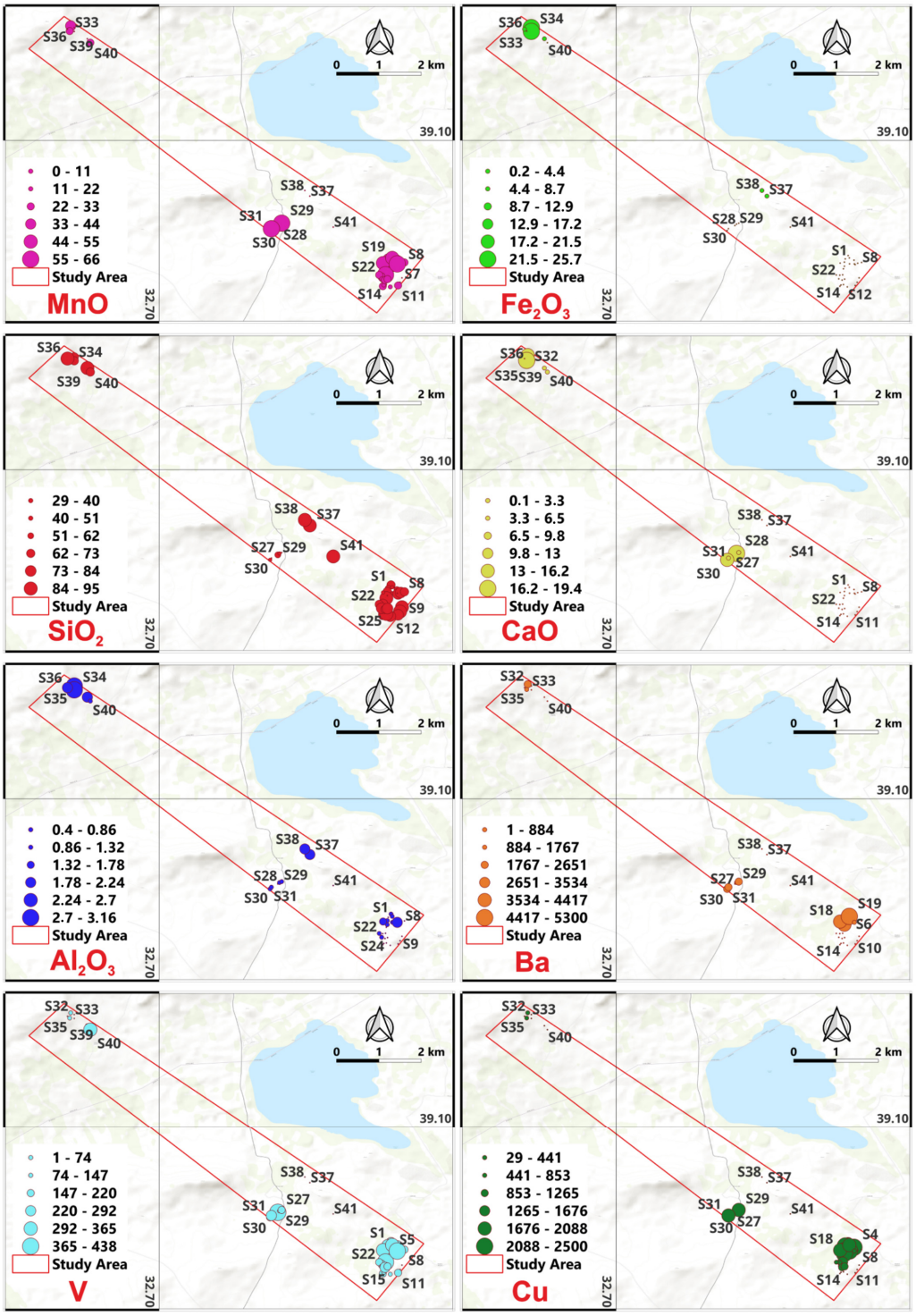


Figure 6. Sample-point maps showing the spatial variation in MnO, SiO_2, CaO, Fe_2O_3, Ba, Cu, V, and Al_2O_3 in the Kulu Mn-bearing samples. Values are shown by graduated symbols at sample locations.

Manganese enrichment in the study area is not homogeneous and is concentrated at specific sample points (Figure 6). High MnO values are particularly observed in Mn-bearing radiolaritic/cherty zones and carbonate-cherty Mn-bearing levels. Low MnO values are mostly observed in samples representing siliceous/radiolaritic or altered lithological zones (Figure 6; Table 1).

Samples with high SiO_2 contents are mostly associated with siliceous/radiolaritic components and do not fully overlap with high MnO values (Figure 6). According to

this distribution, manganese enrichment and the siliceous/radiolaritic component do not show the same chemical behavior. CaO values increase in samples representing carbonate-cherty Mn-bearing levels (Figure 6; Table 1). This indicates that the carbonate component is not homogeneously distributed across the area and becomes prominent in certain sample groups.

Fe_2O_3 values increase particularly in altered or lithologically distinct samples, unlike the main sample group enriched in MnO (Figure 6). Ba, Cu, and V values increase at some sample points enriched in MnO (Figure 6). Ba, Cu, and V values do not show a continuous distribution throughout the study area, but occur as local enrichments at specific locations. The Al_2O_3 distribution does not show a clear overlap with MnO-rich sample points (Figure 6). Relatively high Al_2O_3 values are mostly associated with altered or lithologically differentiated samples. The sample-point-based spatial evaluation indicates that the Kulu samples do not show a uniform and homogeneous distribution, and that distinct chemical differences exist among manganese enrichment, the siliceous/radiolaritic component, carbonate-cherty levels, and altered zones (Figure 6; Table 1).

5. Discussion

5.1. Lithological and Mineralogical Controls on Mn Enrichment

Manganese (Mn) mineralizations are widespread in Türkiye and have been described in different geotectonic settings ranging from the Triassic to the Oligocene [38]. These deposits are largely associated with the closure of the Neo-Tethys Ocean and the subsequent tectonic evolution, and are evaluated together with mélange formation, radiolarian-chert deposition, and basin-margin accumulations [18,39]. Manganese deposits in Türkiye occur mainly along major suture zones, including the Paleo-Tethys, the Karakaya Complex, and the northern and southern branches of the Neo-Tethys Ocean [40]. Along the İzmir–Ankara–Erzincan Suture Zone, manganese oxide occurrences associated with radiolarian cherts are widely observed within ophiolitic mélanges. In such radiolarite/chert-associated Mn oxide occurrences, Mn and Si components are prominent, whereas Al and Fe contributions may remain limited in most samples [16,17,41].

The manganese mineralization in the Kulu area is observed in association with siliceous, carbonate, and ophiolitic rock assemblages within the Dereköy Ophiolitic Mélange. This unit is a complex mélange assemblage containing diabase, serpentinite, mafic rock products, radiolarite/chert and limestone blocks, together with different sedimentary rock slices [20,29]. In the field, the Mn-bearing zones are distinguished by their dark blackish-brown colors and occur locally as vein/filling forms following fractures and cracks, as well as irregular and lenticular masses. The occurrence of Mn-bearing levels together with reddish-brown siliceous/cherty rocks indicates that the mineralization is associated with radiolaritic-siliceous host rocks. The Kızıldağ, Burunağıl, and Madentepe areas occur within the same general geological framework, particularly within the Dereköy Ophiolitic Mélange, and along lithological contacts related to this unit. The available surface data do not directly indicate a continuous ore-body continuity among these three areas. Therefore, the Kızıldağ, Burunağıl, and Madentepe mineralizations are evaluated as mineralization areas that developed within the same regional geological setting but are exposed separately at the surface. Manganite, pyrolusite, and local braunite identified by XRD and ore microscopy in the study area represent the Mn oxide/oxyhydroxide assemblage observed in the surface/near-surface samples from Kulu. Based on the surface samples, these minerals were not directly interpreted as primary precipitation minerals. The fact that Mn oxide minerals may occur as fine-grained, poorly crystalline, and mixed phases requires careful evaluation of mineral identifications [35]. The widespread occurrence of quartz together with Mn minerals in the XRD patterns supports the association of the

mineralization with siliceous/radiolaritic-cherty components. Locally observed calcite indicates a limited carbonate gangue or carbonate-cherty level contribution. A distinct Ba–Mn oxide phase of the psilomelane/romanechite type [35] was not clearly distinguished in the XRD patterns. Therefore, Ba enrichment was evaluated in terms of trace element behavior accompanying the Mn-bearing phases rather than as a separate mineral phase designation [42,43]. These findings indicate that the Kulu manganese mineralization is not represented by a single and homogeneous ore lithology, but shows a heterogeneous character varying with radiolaritic/cherty, carbonate-cherty, siliceous, and altered components. Mineralogical interpretations were not based solely on mineral phase names, but were evaluated together with lithological position, gangue minerals, and major oxide–trace element relationships.

5.2. Element Associations and Geochemical Constraints

Comparisons based on MnO contents showed no statistically significant difference among the Kızıldağ (S1–S26), Burunağıl (S27–S31, S37, S38, and S41), and Madentepe (S32–S36, S39, and S40) sampling areas. The p values obtained from one-way ANOVA, Welch ANOVA, and Kruskal–Wallis tests were above 0.05, indicating that MnO enrichment in this dataset is not restricted to a single sampling area. Although the Kızıldağ, Burunağıl, and Madentepe areas are exposed at the surface as separate mineralization areas, they were evaluated together because they occur within the same regional geological setting.

To evaluate the manganization trend in the study area, relationships between MnO and selected major oxides and trace elements were examined using Spearman correlation analysis (Figure 7). A very strong negative relationship was determined between MnO and SiO_2 ($\rho = -0.89$). This relationship indicates that the siliceous/radiolaritic component relatively decreases in Mn-rich samples and that MnO and SiO_2 behave in opposite directions within the dataset.

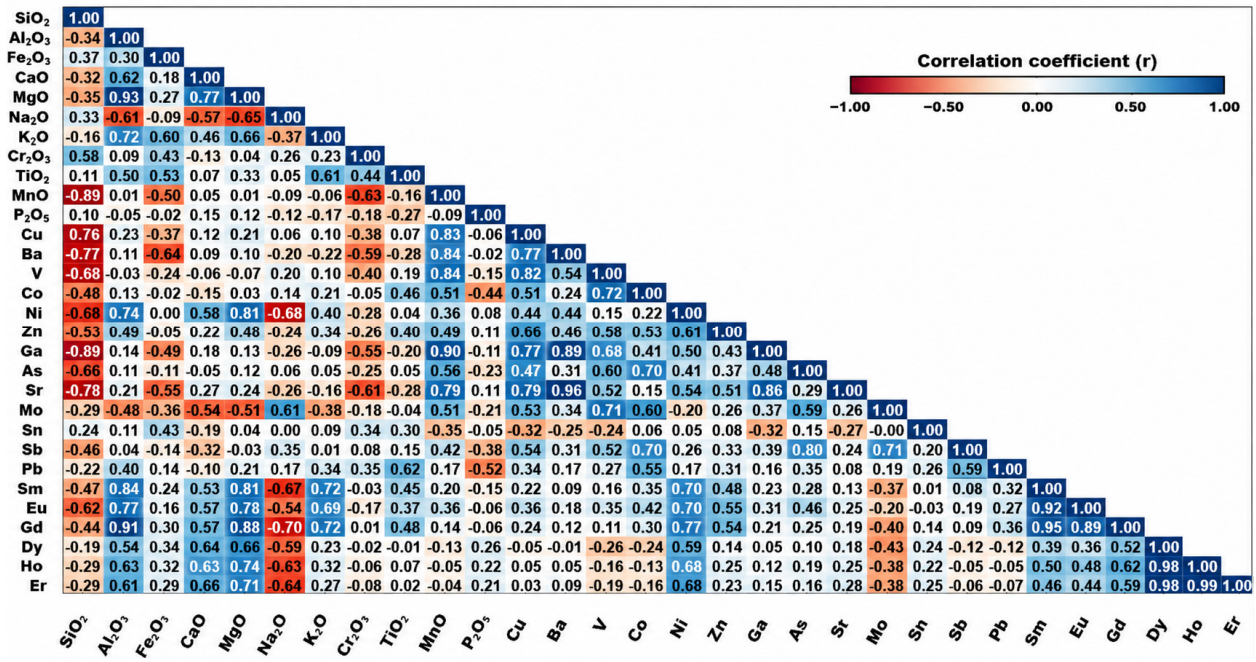


Figure 7. Spearman correlation matrix among major oxides, trace elements, and rare earth elements in the Kulu manganese samples.

The same trend is also clearly observed in the MnO–SiO_2 bivariate plot. The R^2 value of 0.83 obtained from linear regression demonstrates that this inverse relationship is pronounced within the dataset (Figure 8). MnO also shows strong positive relationships

with some trace elements. The strongest positive relationship was determined between MnO and Ga (ρ = 0.90), followed by MnO–Ba (ρ = 0.84), MnO–V (ρ = 0.84), MnO–Cu (ρ = 0.83), and MnO–Sr (ρ = 0.79). Ga, Ba, V, Cu, and Sr tend to increase together in Mn-rich samples. The positive relationships of MnO with Ba, Cu, and V are also supported by the bivariate plots (Figure 8).

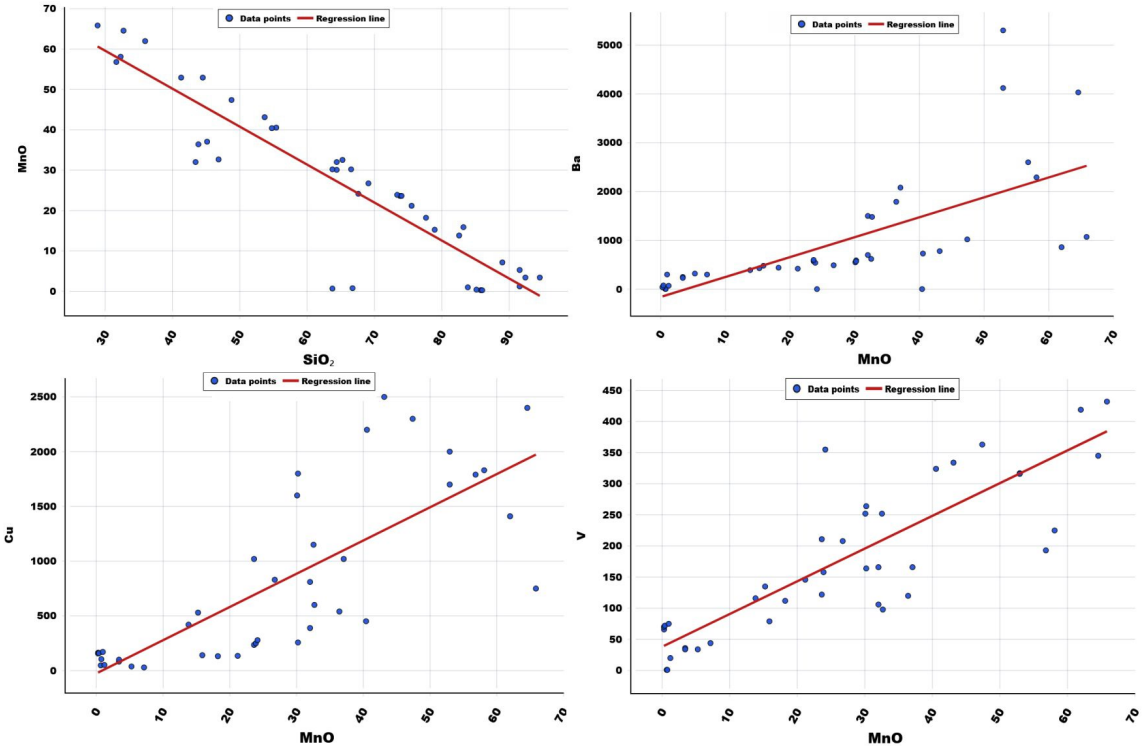


Figure 8. Bivariate regression plots of MnO versus SiO_2, Ba, Cu, and V in the Kulu manganese samples.

Multi-element geochemical datasets define a multidimensional chemical space. Multivariate methods such as PCA can be used to identify geological/geochemical patterns within such datasets [44]. PCA was performed on the combined geochemical dataset after Z-score standardization, and the results were evaluated together with the Spearman correlation matrix and MnO-based bivariate plots. The first two principal components explain 59.98% of the total variance, with PC1 accounting for 34.53% and PC2 for 25.45%. These results show that a substantial part of the geochemical variability in the dataset is represented on the first two axes (Table 5).

In the PCA biplot, the PC1 axis reflects a Fe–Al–Mg-rich lithological/alteration component associated particularly with Al_2O_3, Fe_2O_3, MgO, Ni, As, Sn, and rare earth elements such as Sm, Gd, Dy, Ho, and Er. Cr_2O_3 accompanies this group at moderate to high levels, whereas K_2O and TiO_2 occur within the same general separation with weaker loadings. The clear separation of samples such as S33 and S34 in this direction indicates that, in these samples, a lithological/host-rock component enriched in Fe–Al–Mg and rare earth elements is more influential than Mn enrichment. This separation may also be evaluated together with the contribution of gangue or alteration components. The positioning of some samples close to the SiO_2 direction indicates that the radiolaritic component represents one of the important distinctions in the dataset (Figure 9). The PC2 axis is more closely associated with manganization. The clearly positive position of the MnO vector on PC2, together with the positioning of Ba, Cu, V, Ga, Zn, Co, Pb, and Sr in the same general direction as MnO, indicates that this axis reflects trace element behavior accompanying Mn enrichment. These results are also consistent with the Spearman correlation results. This distribution is

consistent with the Spearman correlation results, which show strong positive relationships between MnO and Ga, Ba, V, Cu, and Sr.

Table 5. Component loadings of major oxides, trace elements, and rare earth elements for the first four principal components of the Z-score standardized Kulu Mn-bearing sample dataset.

Element	PC1	PC2	PC3	PC4
SiO_2	−0.28382	−0.88676	−0.18506	0.149999
Al_2O_3	0.928595	−0.07058	−0.08942	0.075739
Fe_2O_3	0.844287	−0.35103	−0.34432	−0.23967
CaO	0.261449	0.085534	0.810364	−0.11208
MgO	0.809333	−0.21019	0.370519	−0.10977
Na_2O	−0.63774	−0.21592	−0.64911	−0.12665
K_2O	0.453876	−0.03622	−0.32451	0.399984
Cr_2O_3	0.660493	−0.44275	−0.45079	−0.27475
TiO_2	0.386536	0.122871	−0.18076	0.73916
MnO	−0.08064	0.953482	0.065175	−0.05304
P_2O_5	−0.09505	−0.15204	0.461559	−0.01756
Cu	−0.12601	0.832658	−0.12107	−0.3424
Ba	0.062644	0.840458	0.143798	−0.111
V	−0.17405	0.81458	−0.29662	0.213998
Co	0.0727	0.739809	−0.53294	0.252551
Ni	0.814761	0.307652	0.229477	−0.37623
Zn	0.152581	0.789268	−0.15827	0.04311
Ga	0.138579	0.830405	0.333295	−0.07793
As	0.773553	−0.08629	−0.48139	−0.31204
Sr	0.047186	0.68632	0.614684	−0.33807
Mo	−0.44383	0.413738	−0.4636	−0.36569
Sn	0.802392	−0.27736	−0.37908	−0.34663
Sb	0.398735	0.333938	−0.6684	−0.48754
Pb	0.164069	0.659607	−0.32762	0.054546
Sm	0.854104	0.316103	−0.0369	0.41373
Eu	0.711645	0.396539	−0.09923	0.43134
Gd	0.845726	0.217438	−0.00909	0.369773
Dy	0.945337	−0.17168	0.182472	−0.03469
Ho	0.951263	−0.14794	0.200801	−0.06952
Er	0.940932	−0.1442	0.235663	−0.10822

In the biplot, the close positioning of samples S17, S18, and S19 to the MnO vector together with the Ba, Ga, Zn, Cu, and V vectors indicates that manganization and associated trace element enrichment are pronounced in these samples. Co, Pb, and Sr also plot within the positive PC2 field, but show a broader distribution relative to MnO. Samples S33 and S34 are separated toward the field defined by variables such as Fe_2O_3, Al_2O_3, MgO, Sn, Ho, Dy, and Er. This separation indicates that not only Mn enrichment but also Fe–Al–Mg-rich lithological or alteration components are effective within the dataset (Figure 9). PC3 may reflect a carbonate/gangue component, particularly through the CaO loading and the contribution of Sr. PC4 indicates a more limited lithological separation associated with the TiO_2 loading. Because most of the total variance is concentrated on PC1 and PC2, the interpretation mainly considered these two axes.

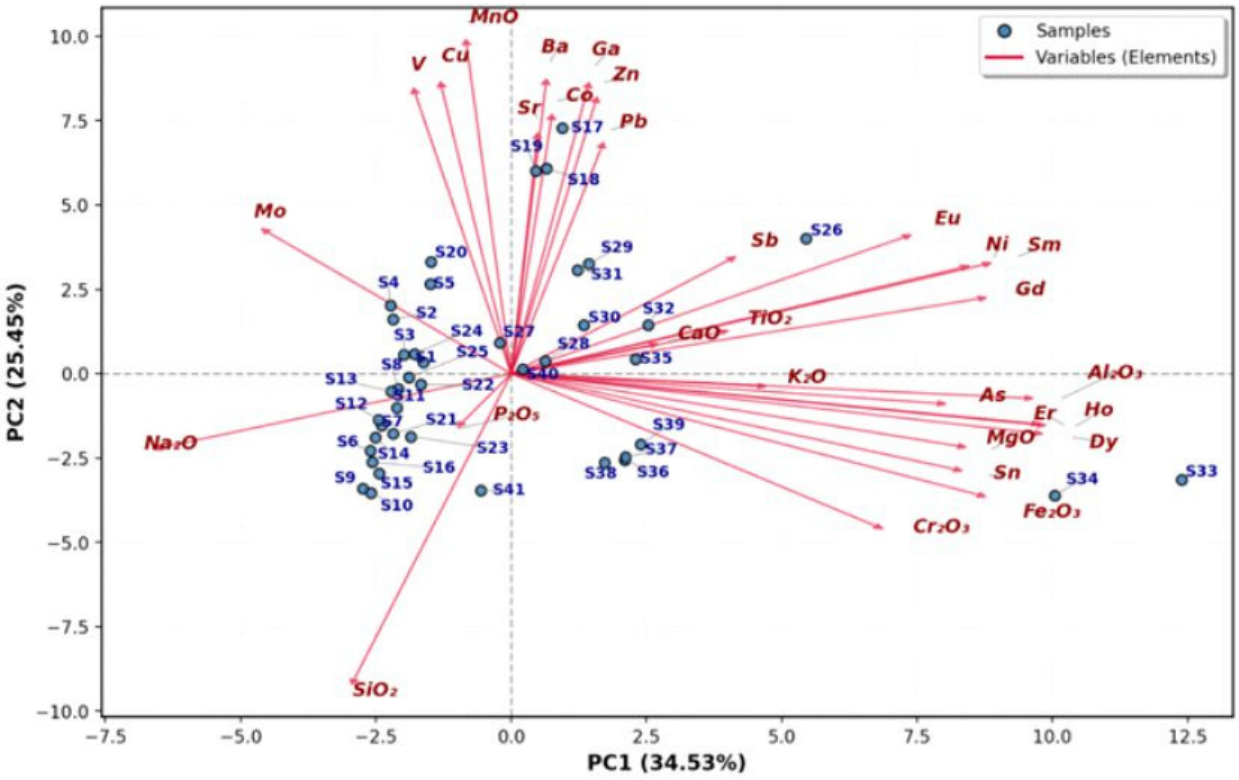


Figure 9. PCA biplot of major oxide, trace element, and rare earth element data for the Kulu manganese samples.

Spearman correlation shows a very strong negative relationship between MnO and SiO_2 ($\rho = -0.89$), which is one of the main findings supporting the PCA interpretation. Although the Mn-bearing zones are spatially associated with radiolaritic/cherty units in the field, MnO and SiO_2 do not show enrichment in the same direction in the chemical composition of the samples. As MnO increases, SiO_2 generally tends to decrease. Therefore, in this dataset, SiO_2 does not behave as an enrichment component accompanying manganization, but rather as an opposing chemical component representing the radiolaritic/cherty host-rock component.

The factor analysis results indicate that the geochemical variables in the study area are separated around three main compositional trends. The first trend represents the radiolaritic component characterized by SiO_2, the second trend represents the Mn-bearing ore component accompanied by MnO together with Cu, Ba, and V, and the third trend represents the detrital/aluminosilicate contribution characterized by Al_2O_3. The strong negative relationship between SiO_2 and MnO shows that Mn enrichment is geochemically separated from the siliceous host-rock component. In contrast, the positive relationships of MnO with Cu, Ba, and V indicate that these elements accompany the Mn-bearing zones and vary in the same direction as MnO. The distinct behavior of Al_2O_3 supports the interpretation that Mn enrichment is not controlled in the same direction as the detrital/aluminosilicate component (Figure 10).

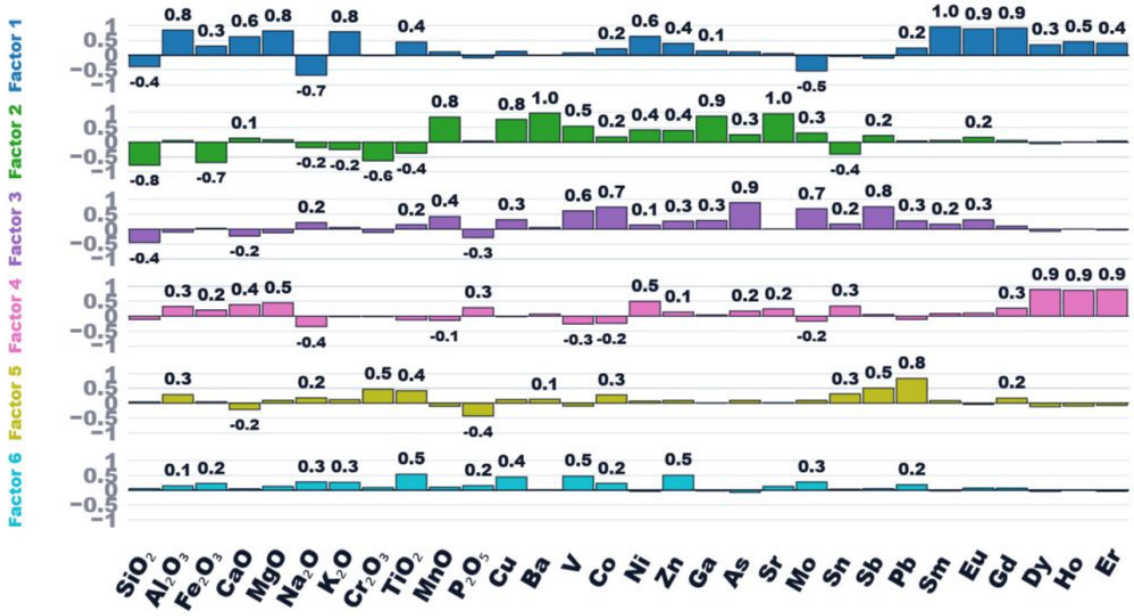


Figure 10. Factor loadings of major oxide, trace element, and rare earth element variables in the Kulu manganese samples.

The HCA dendrogram shows that the geochemical variables are grouped into several main clusters. The MnO–Ba–Sr–Ga–Zn–Cu–V association observed in the dendrogram represents the trace element behavior accompanying Mn enrichment (Figure 11). The occurrence of MnO in the same general direction as Ba, Ga, Zn, Cu, V, and Sr in PCA, together with the strong positive correlations of MnO particularly with Ba, V, Cu, Ga, and Sr in the Spearman correlation analysis, supports this group. In contrast, SiO_2 does not cluster with the MnO-related group and occurs in a different group in the dendrogram. This is also consistent with the very strong negative MnO–SiO_2 relationship observed in the Spearman correlation analysis.

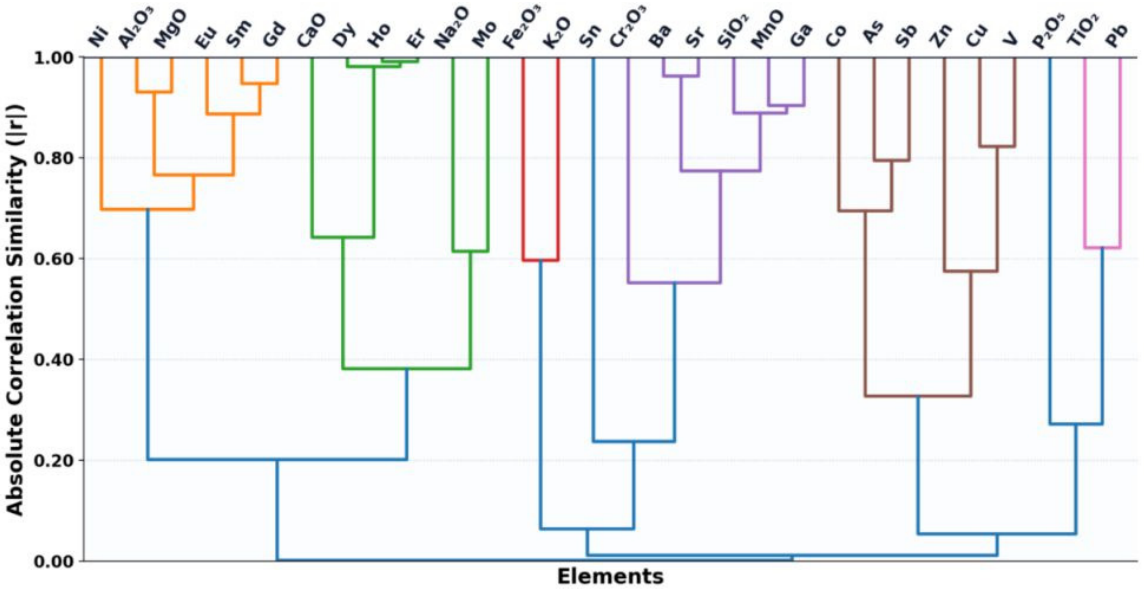


Figure 11. HCA dendrogram showing the hierarchical clustering relationships among major oxide, trace element, and rare earth element variables in the Kulu manganese samples.

In the dendrogram, the Al_2O_3–MgO–Ni–Eu–Sm–Gd and CaO–Dy–Ho–Er variables form a separate group distinct from the main MnO-related group. Fe_2O_3, K_2O, Sn, TiO_2, and Pb variables are also positioned separately from the MnO-centered group. The Co–As–Sb variables form a separate trace element subgroup distinct from the MnO–Ba–Sr–Ga–Zn–Cu–V main group (Figure 11). In manganese deposits associated with radiolaritic/ophiolitic settings, the negative relationship between SiO_2 and MnO is related to the dilution effect of siliceous host rock, radiolaritic chert, or detrital/siliceous components on mineralization [45]. The inverse behavior of MnO with SiO_2, in contrast to its positive relationships with Cu, Ba, V, Ga, and Sr, indicates that Mn enrichment is not limited only to an increase in MnO, but that some trace elements also systematically accompany the Mn-bearing zones. In Mn–Fe deposits, elements such as As, Ba, Cu, Mo, Pb, Sr, V, and Zn have been reported to show enrichment tendencies in oxide ores precipitated from hydrothermal fluids [46]. The lack of full overlap between Al_2O_3 and the MnO–Cu–Ba–V group indicates that manganese mineralization developed through a geochemical process different from the detrital/aluminosilicate component. Al is generally associated with detrital/aluminosilicate input in sedimentary rocks and indicates primary detrital material input into the depositional environment [45,47,48]. Al and Ti are elements with low solubility that can be transported into the depositional environment by rivers as solid particles. Therefore, low or high contents of these elements may indicate relatively low or high input of detrital phases into the depositional environment [41].

5.3. Genetic Implications and Comparison with Related Mn Mineralizations

The formation of manganese deposits is often too complex to be explained by a single process. Sedimentary, volcano-sedimentary, hydrothermal, metamorphic, and supergene processes may have been effective to varying degrees in different deposits [15]. Manganese deposits can be evaluated under different genetic groups, and multiple sources and processes may be involved in their formation [15]. In interpreting manganese mineralization, relying solely on a single mineral phase, one elemental ratio, or one discrimination diagram is not sufficient. Because direct evidence, such as proximity to a spreading center or sedimentation rate, is often not preserved in Fe–Mn deposits, petrographic and geochemical characteristics need to be evaluated together. The combined use of Fe/Ti–Al/(Al+Fe+Mn), Fe/Mn, Fe–Mn–(Co+Ni+Cu), U/Th, and REE data is important for genetic interpretation [49]. The genetic interpretation of the Kulu manganese mineralization was not based on a single dataset; instead, field relationships, lithological position, ore mineralogy, major oxide–trace element geochemistry, multivariate statistical analyses, and comparative deposit data were evaluated together. The MnO–SiO_2 relationship, the trace element association between MnO and Ba–Cu–V–Ga–Sr–Zn, Fe/Mn, Co/Ni, and Co/Zn ratios, and selected geochemical discrimination diagrams were used to discuss the relationship of the Kulu mineralization with hydrothermal, hydrogenetic, and lithological/gangue components. Manganese is a redox-sensitive element whose geochemical behavior is strongly controlled by the redox conditions of the environment [50]. Under oxidizing conditions, dissolved manganese in the form of Mn^{2+} may pass into higher oxidation states and form oxide/oxyhydroxide phases containing Mn^{3+} and Mn^{4+}. Therefore, manganese oxide and oxyhydroxide minerals may precipitate under weakly alkaline marine conditions or weakly acidic freshwater conditions [35,51]. During interaction with surface and groundwater, Mn can be readily mobilized from rocks, may behave as mobile Mn(II) in acidic aqueous systems, and can form numerous Mn oxide/oxyhydroxide minerals under near-surface oxidizing conditions. These minerals are widely found in soils and sediments and may occur as fine-grained aggregates, veins, nodules, crusts, and coatings; they can also participate in oxidation–reduction and cation-exchange reactions. In contrast, under reducing conditions,

manganese may mostly remain as dissolved Mn^{2+} or precipitate as manganese carbonates under suitable carbonate conditions [35,52,53].

The presence of Mn minerals such as manganite, pyrolusite, and braunite in the study area, their association with gangue minerals such as quartz and locally calcite, the marked contrast between MnO and SiO_2, the positive relationships between MnO and some trace elements, and sample groups differentiated in terms of Fe–Al–Mg–Cr are the main features that stand out in the manganese geochemistry of the region. This suggests that the mineralization has a multi-component geochemical character that cannot be explained by a single mineral phase or a single elemental ratio. The manganese data from the Kulu area were discussed in terms of lithological control, MnO–SiO_2 relationships, trace element behavior, mineralogical-textural findings, and geochemical discrimination diagrams. Minerals identified in manganese oxide deposits are not always primary precipitation products, and the mineralogy may change through ageing and recrystallization of initially amorphous Mn oxide phases. Mn oxides in upper oxidized zones may also be of secondary origin [42]. Because Mn oxide minerals commonly occur as fine-grained, poorly crystalline, and mixed phases, their identification is difficult; pyrolusite may also develop as a replacement product of other Mn oxide minerals, especially ramsdellite and manganite, as observed in low-temperature hydrothermal deposits [35]. The occurrence of braunite in only some samples indicates local Mn-phase diversity in the Kulu manganese mineralization. However, due to its limited occurrence, braunite was not used as a decisive indicator in the genetic interpretation. The mineralogical interpretation was based not simply on individual mineral names, but on the evaluation of the Mn oxide/oxyhydroxide mineral assemblage together with its field relationships, lithological context, textural characteristics, and geochemical data. The widespread occurrence of quartz together with manganese minerals in the XRD patterns supports the association of the mineralization with siliceous/radiolaritic-cherty components. The presence of calcite indicates a limited carbonate gangue or carbonate-cherty Mn-bearing level contribution in the system. The Kulu mineralization was not evaluated as a simple mineralization consisting only of Mn oxide phases, but rather as a heterogeneous system in which siliceous/radiolaritic-cherty components, local carbonate contribution, and Mn oxide/oxyhydroxide mineral assemblages developed under surface conditions occur together.

SEM–EDS investigations show that the analyzed Mn-rich phase consists mainly of Mn and O. The very low Si and Ca values in the normalized EDS results indicate that the analyzed point represents a Mn oxide/oxyhydroxide-type phase rather than gangue minerals such as quartz or calcite. In SEM images, these phases are observed locally as platy, rod-like, and aggregate-textured crystal assemblages. The fact that Mn oxide/hydroxide phases may occur as poorly crystalline, chemically variable, and finely intergrown phases requires careful interpretation of SEM–EDS results [36]. Therefore, SEM–EDS data were used as semi-quantitative chemical data supporting the XRD and ore microscopy findings. Ore microscopy, XRD, and SEM–EDS data suggest that the Kulu manganese mineralization is represented in surface/near-surface samples by a Mn-rich mineral assemblage mainly containing manganite and pyrolusite, and locally braunite. This mineral assemblage was not considered as a standalone decisive evidence directly indicating primary hydrothermal precipitation conditions, but rather as the present mineralogical composition that should be evaluated together with field relationships and geochemical data.

Marine manganese oxide deposits may develop as systems in which chemical precipitation, sedimentary accumulation, diagenesis, and hydrothermal contribution are effective in varying proportions, and they are evaluated under different genetic groups according to their formation conditions. Hydrothermal-type manganese oxide deposits generally develop in radiolarian-chert environments associated with seafloor spreading centers,

island-arc systems, and ophiolitic mélanges as a result of the interaction between low-temperature hydrothermal fluids and seawater [13,17,41,54]. Hydrothermal manganese occurrences may be observed either as Mn oxide precipitates associated with hot springs in terrestrial geothermal systems or as sedimentary-exhalative manganese mineralizations in marine environments [42]. Hydrogenetic occurrences refer to systems formed by the slow precipitation of dissolved components directly from seawater or by adsorption onto Mn–Fe oxide surfaces [42,55,56].

In interpreting such deposits, it is important to determine whether hydrothermal and/or volcanic contributions were involved in the mineralization environment. For this purpose, Al and Ti contents are widely used in manganese mineralizations to evaluate the source and depositional environment [41,56]. Al is generally associated with clay-rich or detrital components. High Al values may indicate the contribution of sedimentary/detrital material to the environment during manganese precipitation [51]. Ti, on the other hand, is considered an element that behaves relatively immobile in hydrothermal solutions [57]. Therefore, low Al and Ti values suggest that detrital material input into the environment was limited during manganese precipitation. The Al_2O_3/TiO_2 ratio is also evaluated as being related to volcanic contribution rather than sedimentary transport, weathering, or diagenesis [58–60]. In different mafic volcanic rocks associated with the oceanic crust of the İzmir–Ankara–Erzincan Ocean (N-MORB, E-MORB, OIB, SSZ), Al_2O_3/TiO_2 ratios vary between 8 and 18 [61].

In this study, Al/(Al+Fe+Mn)–Fe/Ti, log Fe/Mn–log Ba, Co/Zn–Co+Ni+Cu, Co+Ni–As+Cu+Mo+Pb+V+Zn, and SiO_2–Al_2O_3 discrimination diagrams were used to evaluate the geochemical character of the samples from the study area (Figure 12).

In the Al/(Al+Fe+Mn)–Fe/Ti diagram [11,49], most of the samples plot within or close to the hydrothermal field (Figure 12a). Mn-rich samples represent the main Mn-bearing group with low Al/(Al+Fe+Mn) values, whereas Fe-rich and Mn-poor samples such as S33 and S34 are separated from this group. Samples S36–S39 are also separated from the main Mn enrichment group by their Mn-poor and relatively Fe–Al-rich character. This distribution is also consistent with the Fe_2O_3–Al_2O_3–MgO–Cr_2O_3-oriented lithological/alteration component observed in PCA.

In the log Fe/Mn–log Ba diagram [11,49], a significant proportion of the samples plot close to the field associated with hydrothermal influence (Figure 12b). In particular, Mn- and Ba-rich samples such as S17, S18, and S19 are also notable for their close positioning to the Ba, Ga, Zn, Cu, and V vectors together with MnO in the PCA. Not all samples cluster in the same field. Fe-rich and Mn-poor samples S33–S34 and S36–S39 are separated from the main Mn-bearing group and reflect lithological/alteration-related heterogeneity within the dataset. High Ba contents in Mn oxides, together with minor concentrations of Fe, Co, Ni, Cu, and Zn, may reflect leaching of organic-rich biogenic sediments or limited barite precipitation in the deeper parts of hydrothermal systems [46,65]. Ba concentrations in hydrothermal solutions are higher than those in seawater due to the effects of volcanic activity and sedimentation [66,67]. The strong positive relationships of Ba, V, Cu, and Sr with MnO also indicate that trace element enrichment in the Mn-bearing zones shows a heterogeneous but distinct trend. This indicates that Mn-rich samples are characterized not only by an increase in MnO, but also by increases in some trace elements. In the samples from the study area, Ba contents range from 1 to 5300 ppm, with an average value of 943.56 ppm for the whole dataset. The average Ba content being higher than the approximately 600 ppm value reported for sedimentary rocks indicates marked Ba enrichment in some samples [68]. In particular, Ba values reaching 4030–5300 ppm in samples S17, S18, and S19 indicate that Ba was also strongly incorporated into the system together with manganization. Similarly, the generally high Ba values in the S28–S32 and

S35 group suggest that sedimentary contribution or fluid–sediment interaction may have been more pronounced in these samples [67]. In Mn–Fe deposits, elements such as As, Ba, Cu, Mo, Pb, Sr, V, and Zn have been reported to show enrichment tendencies in oxide ores precipitated from hydrothermal fluids [46]. Considering the As–Ba–Cu–Li–Mo–Pb–Sb–Sr–V–Zn enrichment trend, it can be regarded as a diagnostic indicator of hydrothermal geochemical influence [42]. The positive relationships between MnO and Ba, Cu, V, Sr, and Zn in the Kulu samples show a trace element distribution consistent with hydrothermal influence.

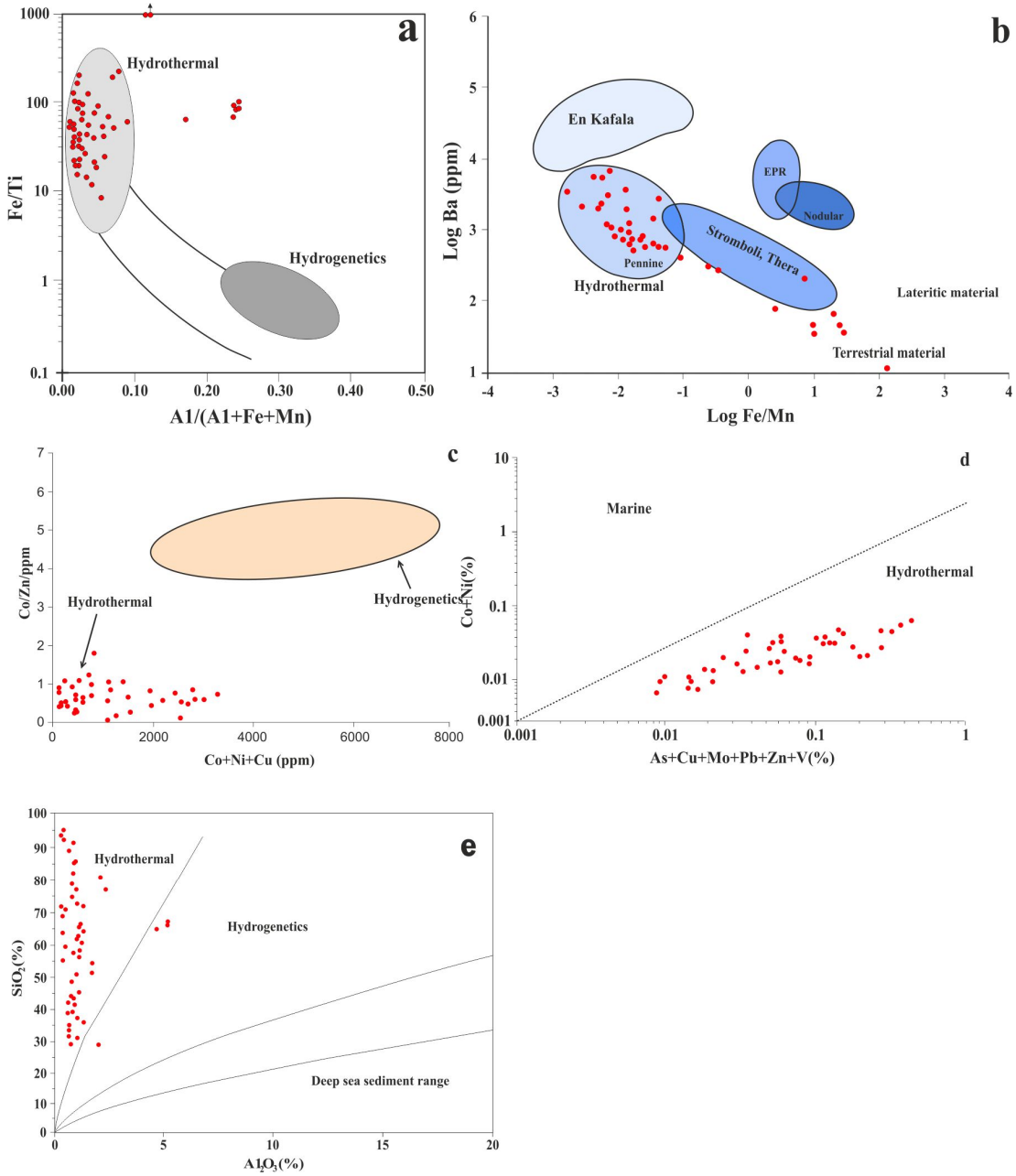


Figure 12. Position of the Kulu Mn-bearing samples on selected geochemical discrimination diagrams. (**a**) Al/(Al+Fe+Mn)–Fe/Ti discrimination diagram [11,49]. (**b**) Log Fe/Mn–log Ba discrimination diagram [11,49]. (**c**) Co/Zn–Co+Ni+Cu discrimination diagram [11,62,63]. (**d**) Co+Ni–As+Cu+Mo+Pb+V+Zn discrimination diagram [11,42]. (**e**) SiO_2–Al_2O_3 discrimination diagram [11,17,62,64].

In the Co/Zn–Co+Ni+Cu diagram [11,62,63], most of the samples plot within or close to the hydrothermal field (Figure 12c). This distribution indicates that the Kulu samples are generally separated from the hydrogenetic field and display a geochemical pattern compatible with hydrothermal influence. Samples S16, S27, S29, S35, and S40 show slight deviations from the main group, reflecting local trace element variability within the dataset. In the Co+Ni–As+Cu+Mo+Pb+V+Zn diagram proposed by [42], the Kulu samples plot in the hydrothermal field, indicating compatibility with hydrothermally influenced Mn oxide/oxyhydroxide systems (Figure 12d). In the SiO_2–Al_2O_3 diagram, most samples plot close to the hydrothermal field, reflecting their high SiO_2 and low Al_2O_3 character (Figure 12e). In this study, the Al–Mn–Fe ternary diagram [69], the Zn–Ni–Co ternary diagram [70], and the Mn–Fe–(Co+Ni+Cu)×10 ternary diagram [55,56,71] were used to distinguish the hydrothermal and hydrogenetic characters of the deposits (Figure 13).

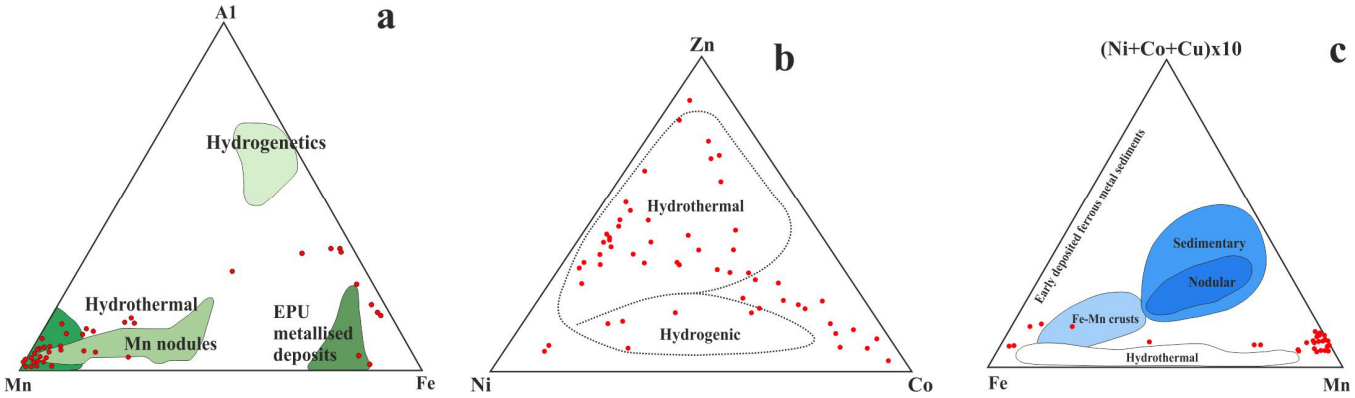


Figure 13. Ternary discrimination diagrams showing the geochemical position of the Kulu Mn-bearing samples in relation to hydrothermal and hydrogenetic fields. (**a**) Al–Mn–Fe ternary diagram [69]. (**b**) Zn–Ni–Co ternary diagram [70]. (**c**) Mn–Fe–(Co+Ni+Cu)×10 ternary diagram [55,56,71].

In this study, the Al–Mn–Fe ternary diagram [69], the Zn–Ni–Co ternary diagram [70], and the Mn–Fe–(Co+Ni+Cu) × 10 ternary diagram [55,56,71] were used to distinguish the hydrothermal and hydrogenetic characters of the deposits (Figure 13).

In the Al–Mn–Fe ternary diagram [69], the Kulu samples are predominantly located close to the Mn apex, around the hydrothermal field, and partly within the Mn nodule field. This position indicates that the samples are Mn-rich and relatively poor in Al and Fe. Their position is more consistent with hydrothermally influenced Mn enrichment than with a hydrogenetic field (Figure 13a). In the Zn–Ni–Co ternary diagram, most samples are positioned away from the Co apex and close to the Ni–Zn trend. This distribution indicates a stronger hydrothermal contribution than hydrogenetic influence in the mineralization [56,70] (Figure 13b). In the Mn–Fe–(Co+Ni+Cu) × 10 diagram [55,56,71], most samples plot close to the Mn apex and show a distribution consistent with the hydrothermal field (Figure 13c). This distribution suggests that the Kulu samples are closer to Mn-rich hydrothermal or hydrothermally influenced chemical precipitation than to slowly growing hydrogenetic Fe–Mn nodule/crust systems. The separation of samples S33–S34 and S36–S39 toward the Fe apex indicates the presence of a Fe-rich lithological/alteration component in the dataset. Hydrogenetic and hydrothermal Mn occurrences can be compared using Co/Ni and Co/Zn ratios [62]. A Co/Ni ratio < 1 is associated with sedimentary character, whereas a Co/Ni ratio > 1 is associated with deep marine environmental influence [67,72,73]. In the Kulu samples, Co/Ni ratios range from approximately 0.001 to 1.77, with an average value of 0.53. The Co/Ni ratio is below 1 in 37 samples, approximately 1 in one sample, and above 1 in only three samples. Co/Zn ratios range from approximately 0.003 to 1.84, with an average value of 0.64. All Co/Zn ratios are below the value of approximately

2.5 proposed for hydrogenetic deposits, indicating that the Kulu samples do not approach the hydrogenetic end-member. In contrast, Co/Zn ratios below 0.15 in samples S29 and S35 suggest that these samples are closest to the hydrothermal end-member. The predominance of Co/Ni ratios below 1 indicates the presence of a sedimentary/marine component in the environment in which the mineralization developed. When Co/Zn ratios, discrimination diagrams, the relationship of MnO with Cu–Ba–V, mineralogical findings, and spatial distribution are evaluated together, the mineralization is interpreted as a heterogeneous Mn mineralization consistent with hydrothermal influence. Seawater is the main medium that enables precipitation and is effective in the formation of hydrogenetic manganese deposits [62,74,75]. These solutions contain amorphous iron and low concentrations of manganese oxide. Their Mn/Fe ratio is approximately 1, Ni and Cu concentrations are greater than 3000 ppm, and they also show negative Ce anomalies [11,62,74,76]. Diagenetic manganese deposits generally have nodular structures [62,74,75] and commonly show a laminated appearance [62,74]. Diagenetic and hydrothermal manganese deposits are characterized by high Mn/Fe ratios and low trace element contents [11,62,77–80].

The Fe/Mn ratio is one of the auxiliary geochemical indicators used in the genetic evaluation of manganese mineralizations. A Fe/Mn ratio of approximately 1 may indicate hydrogenetic manganese deposits, a ratio lower than 0.1 may indicate Mn-rich submarine hydrothermal deposits, and a ratio higher than 10 may indicate Fe-rich systems [11,42,81]. In the Kulu samples, Fe/Mn ratios range from 0.003 to 34.682. In 30 samples, Fe/Mn is <0.1, and these values reflect the low Fe/Mn character of the main Mn-rich sample group, which is consistent with hydrothermal influence. In contrast, Fe/Mn ratios exceed 1 in samples S33, S34, S36, S37, S38, S39, and S41, and these samples represent a Fe-rich altered/lithological component separated from the main Mn-bearing group. The Fe/Mn ratios were not evaluated as a homogeneous genetic indicator for the whole dataset alone, but were considered together with the lithological distinctions of the samples and other geochemical indicators.

Geochemical data from some studies on manganese were compared with the Kulu manganese mineralization. The Kulu manganese mineralization is characterized by high SiO_2, moderate MnO, low Fe_2O_3–Al_2O_3–TiO_2, and marked Cu–V–Ba enrichment (Table 6). The SiO_2 content being close to that of radiolarite-associated areas such as Haymana and Kumluca supports the strong relationship of the mineralization with the siliceous/radiolaritic host-rock component [11,82]. The MnO value is lower than those of areas with higher MnO contents, such as Waziristan, Baby Bare, Sorgun/Eymir, or Arızlı [18,54,67,83].

In contrast, low Fe_2O_3, Al_2O_3, and TiO_2 values indicate that the Kulu samples are separated from Fe-rich hydrogenetic systems or systems with intense detrital contribution [49,62,72]. They are clearly distinguished from Fe-rich examples such as Hazara [84] and Kasımağa [85]. The enrichment in Cu, V, Ba, Ni, and Co values supports a hydrothermally influenced trace element contribution accompanying the Mn-bearing phases [46,65]. One of the main features highlighted in the Kulu samples is their high Cu content. Among the comparative areas, the Cu value of Kulu, at 794.5 ppm, is one of the highest values. The V value is 180.2 ppm, which is higher than those of Haymana, Kasımağa, Eymir, and Kumluca [11,67,82,85]. Although the average Ba content is lower than that of very Ba-rich areas such as Hazara, Baby Bare, Kasımağa, and Kumluca, it is at a level that supports trace element enrichment accompanying the Mn-bearing zones in the Kulu samples [11,54,84,85]. Therefore, the Kulu manganese mineralization can be evaluated as a manganese mineralization associated with radiolarites, marked by hydrothermal influence, and diluted by a siliceous host-rock component.

Table 6. Comparative geochemical data for the Kulu manganese mineralization and selected manganese mineralizations from previous studies.

Deposit/ Area	Country/ Region	Lithology/Deposit Model	SiO_2	TiO_2	Al_2O_3	Fe_2O_3	MnO	MgO	CaO	Na_2O	K_2O	P_2O_5	Ba	V	Co	Ni	Cu	Zn	Pb	Th	Rb	Sr	Y	Nb	Zr	Source
Waziristan	Pakistan	Ophiolite-associated, metachert-hosted submarine hydrothermal/effusive Mn deposit	43.7	0.3	0.7	3.0	45.9	0.6	1.3	0.3	0.2	0.3	415.0	144.0	11.0	36.0	72.0	64.0	49.0	2.0	2.0	—	—	—	—	[83]
Hazara	Pakistan	Hazira Formation-hosted, shallow-marine shelf ferromanganese deposit with mixed hydrothermal–hydrogenetic source	9.4	0.8	12.5	20.3	33.8	0.6	6.4	0.1	0.9	3.7	6304.0	573.0	404.0	305.0	375.0	580.0	2357.0	31.0	24.0	—	—	—	—	[84]
Baby Bare	Northeast Pacific	Stratabound hydrothermal Mn-oxide crust deposit related to low-temperature ridge-flank hydrothermal venting	2.0	0.0	0.3	2.3	48.5	1.6	1.0	0.6	0.2	0.0	7091.7	172.3	135.3	300.7	226.0	123.2	—	1.0	14.2	877.4	10.0	1.5	9.2	[54]
Wakasa	Japan	Bedded chert-hosted stratiform–stratabound submarine hydrothermal Mn oxide deposit	58.2	0.0	0.6	0.9	32.5	0.2	4.2	0.0	0.1	0.1	13.8	258.0	2.0	28.0	50.0	26.0	112.0	2.0	2.0	85.0	5.0	3.0	12.0	[70]
Kasımağa	Türkiye	Basalt–radiolarite–marl-hosted submarine hydrothermal Mn-oxide deposit within pelagic deposits of the Kırşehir Massif ophiolitic series	13.4	0.1	3.0	14.3	40.4	12.7	6.8	0.1	0.2	0.1	2719.4	106.1	49.5	23.0	126.8	63.5	53.5	433.2	5.0	255.0	22.2	11.1	26.9	[85]
Sorgun/ Eymir	Türkiye	Radiolarite-chert-hosted hydrothermal–hydrogenetic volcano-sedimentary Mn mineralization within a Lower Cretaceous ophiolitic complex	16.0	0.0	0.7	0.3	69.9	0.6	2.4	0.0	0.5	0.7	2364.7	132.0	103.5	67.4	80.5	62.5	9.3	0.6	0.8	116.5	8.5	0.2	8.5	[86]
Kumluca	Türkiye	Radiolarite–chert-associated, irregular–lenticular epigenetic hydrothermal Mn-oxide mineralization occurring as seams/fillings in wall-rock cavities and pores	66.8	0.1	1.3	1.6	15.6	2.8	2.0	0.1	0.2	0.1	3723.9	102.0	121.4	189.6	346.8	32.4	15.9	—	5.4	—	10.3	—	14.5	[11]
Haymana	Türkiye	Reddish radiolarite–marl-hosted hydrothermal-type sedimentary Mn mineralization within the Ankara ophiolitic mélange	63.0	0.0	0.7	0.7	29.2	0.2	0.2	0.1	0.1	0.0	1229.4	143.7	23.2	69.4	154.9	66.7	6.5	0.4	2.9	243.4	3.3	0.7	4.0	[82]
Arızlı	Türkiye	Structurally controlled, radiolarian chert–limestone-hosted diagenetic–supergene Mn mineralization within an ophiolitic mélange	4.0	0.0	3.6	0.4	38.5	1.7	6.3	0.6	0.4	0.1	1367.2	96.9	91.5	35.5	178.2	76.5	6.9	—	17.5	118.7	—	—	54.7	[18]
Durmuştepe	Türkiye	Siliceous mudstone-hosted proximal volcano-sedimentary hydrothermal-exhalative Fe–Mn mineralization	23.5	0.1	4.2	32.1	18.0	0.5	12.2	0.1	0.1	0.9	62.3	1222.4	64.5	1743.1	1142.2	344.7	143.7	—	—	—	111.2	4.0	73.4	[34]
Kulu	Türkiye	Radiolarite/chert-associated, hydrothermally influenced Mn mineralization within the Dereköy ophiolitic mélange	64.6	0.0	1.1	2.4	27.0	1.0	2.5	0.1	0.3	0.4	943.6	180.2	58.8	169.5	794.5	95.3	72.5	—	—	179.4	—	—	—	This study

6. Conclusions

In this study, the Kulu manganese mineralization was evaluated using field observations, ore microscopy, XRD, SEM–EDS, major oxide and trace element geochemistry, and spatial data based on sample locations. The findings indicate that the mineralization is not represented by a single and homogeneous ore body, but occurs as Mn-bearing zones associated with radiolaritic/cherty, siliceous/radiolaritic, carbonate-cherty, and locally altered lithological components within the Dereköy ophiolitic mélange.

According to field observations, the Mn-bearing levels occur within radiolaritic/cherty and siliceous host rocks as irregular, lenticular, and locally fracture–crack/void-filling forms. Mineralogically, the surface and near-surface samples are represented mainly by manganite and pyrolusite, locally accompanied by braunite, together with widespread quartz and limited calcite. Because these minerals were identified in surface/near-surface samples, the Mn oxide/oxyhydroxide assemblage was not evaluated as direct evidence of primary hydrothermal precipitation, but rather as the present mineralogical expression of the mineralization.

The geochemical data show marked heterogeneity among the samples. The strong negative relationship between MnO and SiO_2 indicates that Mn enrichment and the siliceous/radiolaritic component behave as opposing chemical components within the dataset. The positive relationships of MnO with Cu, Ba, V, Ga, and Sr indicate that these trace elements are associated with Mn-rich zones. PCA, HCA, factor analysis, and correlation results also support the distinction among the Mn-rich trace element association, the siliceous/radiolaritic component, and the Fe–Al–Mg-rich altered/lithological components.

The spatial evaluation based on sample locations shows that Mn enrichment is not homogeneously distributed across the study area, but is concentrated in specific locations. High MnO values are mostly associated with Mn-bearing radiolaritic/cherty and carbonate-cherty zones. In contrast, samples with low MnO and high Fe/Mn ratios mainly represent altered radiolaritic/cherty, altered mixed lithological, or siliceous/radiolaritic components.

Overall, the Kulu manganese mineralization is interpreted as a radiolarite/chert-associated and lithologically heterogeneous Mn mineralization within the Dereköy ophiolitic mélange. Its lithological position, MnO–SiO_2 contrast, trace element relationships between MnO and Cu–Ba–V–Ga–Sr, low Fe–Al–Ti character in the main Mn-bearing samples, and position in geochemical discrimination diagrams indicate that the mineralization is consistent with hydrothermal influence.

Funding: The financial support for this research was provided by the Scientific Research Projects Coordination Unit of Selçuk University (Project No. 18401129).

Data Availability Statement: The geochemical, XRD, and SEM–EDS data supporting the findings of this study are presented within the manuscript.

Acknowledgments: The author would like to thank the Scientific Research Projects Coordination Unit of Selçuk University. The author would also like to express gratitude to Geological Engineer Sadık Kılıç and Alican Öztürk for their assistance during the project field studies.

Conflicts of Interest: The author declares no conflicts of interest. The funder had no role in the design of the study, in the collection, analyses, or interpretation of data, in the writing of the manuscript or in the decision to publish the results.

Abbreviations

AI	Artificial intelligence
ANOVA	Analysis of variance
Bnt	Braunite
Cal	Calcite
EDS	Energy-dispersive X-ray spectroscopy
HCA	Hierarchical cluster analysis
HF	Hydrofluoric acid
KBM	Kütahya–Bolkardağı Metamorphites
METU MERLAB	Middle East Technical University Central Laboratory
Mnt	Manganite
N-MORB	Normal mid-ocean-ridge basalt
E-MORB	Enriched mid-ocean-ridge basalt
OIB	Ocean island basalt
PCA	Principal component analysis
ppm	Parts per million
Pyl	Pyrolusite
QGIS	Geographic information system software
Qz	Quartz
REE	Rare earth elements
RSD	Relative standard deviation
SEM	Scanning electron microscopy
SEM–EDS	Scanning electron microscopy–energy-dispersive X-ray spectroscopy
SiC	Silicon carbide
SPSS	Statistical Package for the Social Sciences
SSZ	Supra-subduction zone
USGS	United States Geological Survey
wt.%	Weight percent
XRD	X-ray diffraction

References

1. Schmuch, R.; Wagner, R.; Hörpel, G.; Placke, T.; Winter, M. Performance and cost of materials for lithium-based rechargeable automotive batteries. *Nat. Energy* **2018**, *3*, 267–278. [CrossRef]
2. Maisel, F.; Neef, C.; Marscheider-Weidemann, F.; Nissen, N.F. A forecast on future raw material demand and recycling potential of lithium-ion batteries in electric vehicles. *Resour. Conserv. Recycl.* **2023**, *192*, 106920. [CrossRef]
3. U.S. Geological Survey, (USGS). *Mineral Commodity Summaries 2024*; U.S. Geological Survey: Reston, VA, USA, 2024.
4. Zhao, X.; Han, X.; Feng, H.; Liu, L.; Liu, Q.; Liu, G.; Du, B.; Zhu, H. Study on China's manganese resource demand from 2024 to 2035 based on GM-SVR method. *Front. Earth Sci.* **2025**, *13*, 1538908. [CrossRef]
5. Peng, E.; Yang, J.; Wang, Z.; Li, D.; Gao, Y.; Yan, D.; Chen, Y.; Guo, X. Manganese resources in China: An overview of resource status and recent advances in metallogenic models and exploration. *Minerals* **2025**, *15*, 859. [CrossRef]
6. Kerroumi, M.; Karbak, M.; Afaryate, H.; El-Bchiri, A.; Aqil, M.; Manoun, B.; Ghamouss, F. Unveiling electrochemical insights of lithium manganese oxide cathodes from manganese ore for enhanced lithium-ion battery performance. *Electrochim. Acta* **2025**, *509*, 145286. [CrossRef]
7. Helbig, C.; Bradshaw, A.M.; Wietschel, L.; Thorenz, A.; Tuma, A. Supply risks associated with lithium-ion battery materials. *J. Clean. Prod.* **2018**, *172*, 274–286. [CrossRef]
8. Masias, A.; Marcicki, J.; Paxton, W.A. Opportunities and challenges of lithium ion batteries in automotive applications. *ACS Energy Lett.* **2021**, *6*, 621–630. [CrossRef]
9. Sokolova, I.; Nwaila, T.; Ntunka, G.; Klochkov, S.; Michaux, S.; Moscardini, E.; Toro, L.; Ghorbani, Y. From abundant resource to critical commodity: Forecasting manganese supply and assessing its sustainability. *Sustain. Mater. Technol.* **2025**, *44*, e01349. [CrossRef]
10. Kong, C.; Zhao, J.; Li, B.; Wu, C.; Xu, K. Manganese mineral prospectivity mapping based on semi-supervised learning and multi-source geoscientific-sample Wasserstein generative adversarial network (Geo-WGAN) in Songtao of Guizhou, South China. *Ore Geol. Rev.* **2025**, *186*, 106933. [CrossRef]

11. Boztaş, S.; Atakoğlu, O.O.; Yalçın, M.G. The origin and geochemistry of the Kumluca manganese deposit in the South West, Antalya Province, Türkiye: Possibility of derived hydrothermal fluids. *Min. Metall. Explor.* **2025**, *42*, 3161–3193. [CrossRef]
12. Moreira, C.A.; Borges, M.R.; Lira Vieira, G.M.; Malagutti Filho, W.; Fernándes Montanheiro, M.A. Geological and geophysical data integration for delimitation of mineralized areas in supergene manganese deposits. *Geofís. Int.* **2014**, *53*, 201–212. [CrossRef]
13. Roy, S. Genetic diversity of manganese deposition in the terrestrial geological record. In *Manganese Mineralization: Geochemistry and Mineralogy of Terrestrial and Marine Deposits*; Nicholson, K., Hein, J.R., Bühn, B., Dasgupta, S., Eds.; Special Publication 119; Geological Society: London, UK, 1997; pp. 5–27. [CrossRef]
14. Shah, M.T.; Moon, C.J. Manganese and ferromanganese ores from different tectonic settings in the NW Himalayas, Pakistan. *J. Asian Earth Sci.* **2007**, *29*, 455–465. [CrossRef]
15. Kuleshov, V.N. *Isotope Geochemistry: The Origin and Formation of Manganese Rocks and Ores*; Elsevier: Amsterdam, The Netherlands, 2016.
16. Öztürk, H. Türkiye manganez yatakları: Oluşumları ve tipleri. *Jeol. Mühendisliği Derg.* **1993**, *17*, 24–33.
17. Aydoğan, M.S. The Tafak manganese deposit (Dursunbey-Balıkesir, NW Turkey): Implications for the submarine hydrothermal origin of İzmir-Ankara-Erzincan Neotethyan Ocean. *Arab. J. Geosci.* **2021**, *14*, 2321. [CrossRef]
18. Yalçın, C.; Kara, H. Mineralogical and geochemical characterization of the Arızlı Mn deposit (Afyonkarahisar, Turkey): Evidence for diagenetic and supergene enrichment. *Carpathian J. Earth Environ. Sci.* **2026**, *21*, 71–80. [CrossRef]
19. Akyürek, B.; Duru, M.; Sütçü, Y.F.; Papak, İ.; Şaroğlu, F.; Pehlivan, N.; Gönenç, O.; Granit, S.; Yaşar, T. *1/100,000 Ölçekli Açınsama Nitelikli Türkiye Jeoloji Haritaları, Ankara-F15 Paftası, No: 55*; Maden Tetkik ve Arama Genel Müdürlüğü, Jeoloji Etütleri Dairesi: Ankara, Türkiye, 1997.
20. Atıcı, G.; Dönmez, M.; Çobankaya, M.; Sevin, M.; Gündoğdu-Atakay, E.; Esirtgen, E.; Şimşek, E. *1/100,000 Ölçekli Türkiye Jeoloji Haritaları, Ankara J29 Paftası, No: 209*; Maden Tetkik ve Arama Genel Müdürlüğü, Jeoloji Etütleri Dairesi: Ankara, Türkiye, 2014.
21. Görür, N.; Oktay, F.Y.; Seymen, İ.; Şengör, A.M.C. Paleotectonic evolution of the Tuzgölü Basin complex, Central Turkey: Sedimentary record of a Neo-Tethyan closure. In *The Geological Evolution of the Eastern Mediterranean*; Dixon, J.E., Robertson, A.H.F., Eds.; Geological Society Special Publication 17; Geological Society: London, UK, 1984; pp. 467–482.
22. Dellaloğlu, A.A. Ankara İli-Tuzgölü Arasında Neotetisin Kuzey Kolunun Evrimi (Haymana-Tuzgölü Basenlerinin Stratigrafileri ve Jeotektonik Evrimleri). Ph.D. Thesis, Çukurova Üniversitesi Fen Bilimleri Enstitüsü, Adana, Türkiye, 1997.
23. Çemen, İ.; Göncüoğlu, M.C.; Dirik, K. Structural evolution of the Tuzgölü Basin in Central Anatolia, Turkey. *J. Geol.* **1999**, *107*, 693–706. [CrossRef] [PubMed]
24. Dirik, K.; Erol, O. Tectonomorphologic evolution of Tuzgölü and surrounding area, central Anatolia-Turkey. *Turk. Assoc. Pet. Geol. Spec. Publ.* **2003**, *5*, 27–46.
25. Özcan, A.; Göncüoğlu, M.C.; Turhan, N.; Şentürk, K.; Uysal, Ş.; Işık, A. *Konya-Kadınhanı-Ilgın Dolayının Temel Jeolojisi*; MTA Report No. 9535; Maden Tetkik ve Arama Genel Müdürlüğü: Ankara, Türkiye, 1990; unpublished report.
26. Göncüoğlu, M.C.; Dirik, K.; Erler, A.; Yalınız, K.; Özgül, L.; Çemen, İ. *Tuzgölü Havzası Batı Kısmının Temel Jeolojik Sorunları*; TPAO Report No. 3753; Türkiye Petrolleri Anonim Ortaklığı: Ankara, Türkiye, 1996.
27. Asan, K. Kulu (Konya)-Haymana (Ankara) Yöresi Volkanik Kayaçlarının Jeokimyası, Petrolojisi ve Petrojenezi. Ph.D. Thesis, Selçuk Üniversitesi Fen Bilimleri Enstitüsü, Konya, Türkiye, 2007.
28. Horasan, B.Y. *Investigation of Geology and Geochemistry of Manganese Mineralizations in Burunağıl (Konya)–Bumsuz (Ankara) Regions*; Project No. 18401129; Selçuk University Scientific Research Projects Coordination Office: Konya, Türkiye, 2018.
29. Uğuz, M.; Turhan, N.; Bilgin, A.; Umut, M.; Şen, A.; Acarlar, M. *Kulu (Konya), Haymana (Ankara) ve Kırıkkale Dolayının Jeolojisi*; Maden Tetkik ve Arama Genel Müdürlüğü, Jeoloji Etütleri Dairesi: Ankara, Türkiye, 1999.
30. Bingöl, E.; Akyürek, B.; Korkmazer, B. *Biga Yarımadasının Jeolojisi Ve Karakaya Formasyonunun Bazı Özellikleri*; Cumhuriyetin 50. Yılı Yerbilimleri Kongresi Tebliğleri: Ankara, Türkiye, 1973; pp. 70–77.
31. Rigo de Righi, M.; Cortesini, A. *Regional Studies of the Central Anatolian Basin, Progress Report 1*; Petrol İşleri Genel Müdürlüğü Arşivi: Ankara, Türkiye, 1959; Unpublished report.
32. Reimann, C.; Filzmoser, P.; Garrett, R.G.; Dutter, R. *Statistical Data Analysis Explained: Applied Environmental Statistics with R*; John Wiley & Sons: Chichester, UK, 2008.
33. Jolliffe, I.T.; Cadima, J. Principal component analysis: A review and recent developments. *Philos. Trans. R. Soc. A* **2016**, *374*, 20150202. [CrossRef] [PubMed]
34. Öztürk, A.; Altay, O. Geochemical, REE and multivariate statistical constraints on Fe–Mn mineralization in Durmuştepe area (Maden, Elazığ, Türkiye). *Minerals* **2026**, *16*, 687. [CrossRef]
35. Post, J.E. Manganese oxide minerals: Crystal structures and economic and environmental significance. *Proc. Natl. Acad. Sci. USA* **1999**, *96*, 3447–3454. [CrossRef] [PubMed]
36. Parrotti, D.D.; da Conceição, F.T.; Navarro, G.R.B. The mineralogy, geochemistry and origin of the supergene manganese occurrences in the Southern Minas Gerais, Brazil. *Minerals* **2023**, *13*, 1216. [CrossRef]

37. Sánchez-España, J.; Yusta, I. Coprecipitation of Co^{2+}, Ni^{2+} and Zn^{2+} with Mn(III/IV) oxides formed in metal-rich mine waters. *Minerals* **2019**, *9*, 226. [CrossRef]
38. Öztürk, H. Manganese deposits in Turkey: Distribution, types, and tectonic setting. *Ore Geol. Rev.* **1997**, *12*, 187–203. [CrossRef]
39. Göncüoğlu, M.C.; Sayıt, K.; Uzunçimen Keçeli, S. Evolution of the Neotethyan branches in the Eastern Mediterranean: Petrology and ages of oceanic basalts. *Turk. J. Earth Sci.* **2015**, *24*, 249–279. [CrossRef]
40. Öztürk, H.; Cansu, Z.; Hacılar, F.; Bolton, B. Geochemistry of the Oligocene-hosted manganese ores and the host sediments in the Thrace Basin, Türkiye: Implications for genesis and exploration of the Paratethya. *J. Geochem. Explor.* **2025**, *272*, 107707. [CrossRef]
41. Aydoğan, S. Cihanpaşa (Yozgat) bölgesinin güney kesimindeki manganez cevherleşmesinin jeokimyasal özellikleri ve kökeni. *Türkiye Jeol. Bül.* **2022**, *65*, 1–34. [CrossRef]
42. Nicholson, K. Contrasting mineralogical-geochemical signatures of manganese oxides: Guides to metallogenesis. *Econ. Geol.* **1992**, *87*, 1253–1264. [CrossRef]
43. Dekov, V.; Maynard, J.; Kamenov, G.; Rouxel, O.; Lalonde, S.; Juranov, S. Origin of the Oligocene manganese deposit at Obrochishte (Bulgaria): Insights from C, O, Fe, Sr, Nd, and Pb isotopes. *Ore Geol. Rev.* **2020**, *122*, 103550. [CrossRef]
44. Grunsky, E.C.; de Caritat, P. State-of-the-art analysis of geochemical data for mineral exploration. *Geochem. Explor. Environ. Anal.* **2020**, *20*, 217–232. [CrossRef]
45. Lotfi, M.; Kahrazehi, M.; Ghaderi, M. Geochemistry and origin of Dehoo manganese deposit, south Zahedan, southeastern Iran. *Arab. J. Geosci.* **2017**, *10*, 142. [CrossRef]
46. Şaşmaz, A.; Türkyılmaz, B.; Öztürk, N.; Yavuz, F.; Kumral, M. Geology and geochemistry of Middle Eocene Maden complex ferromanganese deposits from the Elazığ–Malatya region, eastern Turkey. *Ore Geol. Rev.* **2014**, *56*, 352–372. [CrossRef]
47. Murray, R.W.; Jones, D.L.; Buchholtz ten Brink, M.R. Diagenetic formation of bedded chert: Evidence from chemistry of the chert-shale couplet. *Geology* **1992**, *20*, 271–274. [CrossRef]
48. Ganno, S.; Njiosseu, E.L.T.; Kouankap, N.G.D.; Djoukouo, S.A.; Moudioh, C.; Ngnotue, T.; Nzenti, J.P. A mixed seawater and hydrothermal origin of superior-type banded iron formation (BIF)-hosted Kouambo iron deposit, Palaeoproterozoic Nyong series, Southwestern Cameroon: Constraints from petrography and geochemistry. *Ore Geol. Rev.* **2017**, *80*, 860–875. [CrossRef]
49. Boström, K. Genesis of ferromanganese deposits—Diagnostic criteria for recent and old deposits. In *Hydrothermal Processes at Seafloor Spreading Centers*; Rona, P.A., Boström, K., Laubier, L., Smith, K.L., Eds.; Springer: Boston, MA, USA, 1983; pp. 473–489. [CrossRef]
50. Lovley, D.R. Fe(III) and Mn(IV) reduction. In *Environmental Microbe-Metal Interactions*; American Society for Microbiology: Washington, DC, USA, 2000; pp. 1–30. [CrossRef]
51. Maynard, J.B. The chemistry of manganese ores through time: A signal of increasing diversity of Earth-surface environments. *Econ. Geol.* **2010**, *105*, 535–552. [CrossRef]
52. Polgári, M.; Okita, P.M.; Hein, J.R. Stable isotope evidence for the origin of the Urkut manganese ore deposit, Hungary. *J. Sediment. Res.* **1991**, *61*, 384–393. [CrossRef]
53. Okita, P.M.; Shanks, W.C. Origin of stratiform sediment-hosted manganese carbonate ore deposits: Examples from Molango, Mexico, and TaoJiang, China. *Chem. Geol.* **1992**, *99*, 139–163. [CrossRef]
54. Fitzgerald, C.E.; Gillis, K.M. Hydrothermal manganese oxide deposits from Baby Bare seamount in the Northeast Pacific Ocean. *Mar. Geol.* **2006**, *225*, 145–156. [CrossRef]
55. Bonatti, E.; Kraemer, T.; Rydel, H. Classification and genesis of submarine iron-manganese deposits. In *Ferromanganese Deposits on the Ocean Floor*; Horn, D.R., Ed.; National Science Foundation: Washington, DC, USA, 1972; pp. 149–166.
56. Crerar, D.A.; Namson, J.; Chyi, M.S.; Williams, L.; Feigenson, M.D. Manganiferous cherts of the Franciscan assemblage: 1. General geology, ancient and modern analogues, and implications for hydrothermal convection at oceanic spreading centers. *Econ. Geol.* **1982**, *77*, 519–540. [CrossRef]
57. Sugisaki, R. Relation between chemical composition and sedimentation rate of Pacific Ocean-floor sediments deposited since the middle Cretaceous: Basic evidence for chemical constraints on depositional environments of ancient sediments. *J. Geol.* **1984**, *92*, 235–259. [CrossRef]
58. Hayashi, K.I.; Fujisawa, H.; Holland, H.D.; Ohmoto, H. Geochemistry of 1.9 Ga sedimentary rocks from northeastern Labrador, Canada. *Geochim. Cosmochim. Acta* **1997**, *61*, 4115–4137. [CrossRef] [PubMed]
59. Sugitani, K.; Horiuchi, Y.; Adachi, M.; Sugisaki, R. Anomalously low Al_2O_3/TiO_2 ratios for Archean cherts from the Pilbara Block, Western Australia—Possible evidence for extensive chemical weathering on the early Earth. *Precambrian Res.* **1996**, *80*, 49–76. [CrossRef]
60. Gao, J.; Yang, R.; Xu, H.; Zhang, X.; Feng, K.; Zheng, L. Genesis of Permian sedimentary manganese deposits in Zunyi, Guizhou Province, SW China: Constraints from geology and elemental geochemistry. *J. Geochem. Explor.* **2018**, *192*, 142–154. [CrossRef]
61. Aldanmaz, E.; Yalınız, M.K.; Güçtekin, A.; Göncüoğlu, M.C. Geochemical characteristics of mafic lavas from the Neotethyan ophiolites in western Turkey: Implications for heterogeneous source contribution during variable stages of ocean crust generation. *Geol. Mag.* **2008**, *145*, 37–54. [CrossRef]

62. Toth, J.R. Deposition of submarine crusts rich in manganese and iron. *Geol. Soc. Am. Bull.* **1980**, *91*, 44–54. [CrossRef]
63. Dzemua, G.L.; Gleeson, S.A. Petrography, mineralogy, and geochemistry of the Nkamouna serpentinite: Implications for the formation of the cobalt-manganese laterite deposit, Southeast Cameroon. *Econ. Geol.* **2012**, *107*, 25–41. [CrossRef]
64. Wonder, J.D.; Spry, P.G.; Windom, K.E. Geochemistry and origin of manganese-rich rocks related to iron formation and sulfide deposits, western Georgia. *Econ. Geol.* **1988**, *83*, 1070–1081. [CrossRef]
65. Hein, J.R.; Schulz, M.S.; Dunham, R.E.; Stern, R.J.; Bloomer, S.H. Diffuse flow hydrothermal manganese mineralization along the active Mariana and southern Izu-Bonin arc system, western Pacific. *J. Geophys. Res.* **2008**, *113*, B08S14. [CrossRef]
66. Monnin, C.; Wheat, C.G.; Dupré, B.; Elderfield, H.; Mottl, M.J. Barium geochemistry in sediment pore waters and formation waters of the oceanic crust on the eastern flank of the Juan de Fuca Ridge (ODP Leg 168). *Geochem. Geophys. Geosyst.* **2001**, *2*, 1008. [CrossRef]
67. Öksüz, N. Geochemistry and the origin of manganese mineralizations in Derbent (Yozgat) region. *Bull. Earth Sci. Appl. Res. Cent. Hacet. Univ.* **2011**, *32*, 213–234.
68. Krauskopf, K.B. *Introduction to Geochemistry*, 2nd ed.; McGraw-Hill: New York, NY, USA, 1979.
69. Bamba, T. The Tokoro Belt: A tectonic unit of the central axial zone of Hokkaido. *J. Fac. Sci. Hokkaido Univ. Ser. IV Geol. Mineral.* **1984**, *21*, 75–95.
70. Choi, J.H.; Hariya, Y. Geochemistry and depositional environment of Mn oxide deposits in the Tokoro Belt, northeastern Hokkaido, Japan. *Econ. Geol.* **1992**, *87*, 1265–1274. [CrossRef]
71. Li, R.-Z.; Jiang, S.; Long, P.; Long, T.; Ding, D.-Q.; Zhao, L.-N.; Zhang, Y.; Huang, Q. Metallogenic mechanisms of the Lower Triassic Dongping sedimentary manganese deposit in the South China Block: Mineralogical and geochemical evidence. *Minerals* **2025**, *15*, 847. [CrossRef]
72. Fernández, A.; Moro, M. Origin and depositional environment of Ordovician stratiform iron mineralization from Zamora (NW Iberian Peninsula). *Miner. Depos.* **1998**, *33*, 606–619. [CrossRef]
73. Delian, F. *Geological and Geochemical Research of the Manganese Ore Bed*; Weather Publishing Press: Beijing, China, 1994.
74. Hein, J.R.; Schulz, M.S.; Gein, L.M. Central Pacific cobalt-rich ferromanganese crusts: Historical perspective and regional variability. In *Geology and Offshore Mineral Resources of the Central Pacific Basin*; Springer: New York, NY, USA, 1992; pp. 261–283. [CrossRef]
75. Hein, J.R.; Koschinsky, A.; Halbach, P.; Manheim, F.T.; Bau, M.; Kang, J.K.; Lubick, N. Iron and manganese oxide mineralization in the Pacific. In *Manganese Mineralization: Geochemistry and Mineralogy of Terrestrial and Marine Deposits*; Nicholson, K., Hein, J.R., Bühn, B., Dasgupta, S., Eds.; Special Publication 119; Geological Society: London, UK, 1997; pp. 123–138. [CrossRef]
76. Ingram, B.L.; Hein, J.R.; Farmer, G.L. Age determinations and growth rates of Pacific ferromanganese deposits using strontium isotopes. *Geochim. Cosmochim. Acta* **1990**, *54*, 1709–1721. [CrossRef]
77. Usui, A.; Nishimura, A. Submersible observations of hydrothermal manganese deposits on the Kaikata Seamount, Izu-Ogasawara (Bonin) Arc. *Mar. Geol.* **1992**, *106*, 203–216. [CrossRef]
78. Hein, J.R.; Spinardi, F.; Okamoto, N.; Mizell, K.; Thorburn, D.; Tawake, A. Critical metals in manganese nodules from the Cook Islands EEZ: Abundances and distributions. *Ore Geol. Rev.* **2015**, *68*, 97–116. [CrossRef]
79. Klinkhammer, G.P.; Heggie, D.T.; Graham, D.W. Metal diagenesis in oxic marine sediments. *Earth Planet. Sci. Lett.* **1982**, *61*, 211–219. [CrossRef]
80. Manheim, F.T.; Lane-Bostwick, C.M. Cobalt in ferromanganese crusts as a monitor of hydrothermal discharge on the Pacific seafloor. *Nature* **1988**, *335*, 59–62. [CrossRef]
81. Oygür, V. Implications on geology, genesis and origin of Çayırlı manganese deposit, Ankara, Central Anatolia. *Bull. Miner. Res. Explor.* **1990**, *110*, 29–43.
82. Karakuş, A.; Yavuz, B.; Koç, S. Mineralogy and major-trace element geochemistry of the Haymana manganese mineralizations, Ankara, Turkey. *Geochem. Int.* **2010**, *48*, 1014–1027. [CrossRef]
83. Shah, M.T.; Khan, A. Geochemistry and origin of Mn deposits in the Waziristan ophiolite complex, North Waziristan, Pakistan. *Miner. Depos.* **1999**, *34*, 697–704. [CrossRef]
84. Shah, M.T.; Moon, C.J. Mineralogy, geochemistry and genesis of the ferromanganese ores from Hazara area, NW Himalayas, northern Pakistan. *J. Asian Earth Sci.* **2004**, *23*, 1–15. [CrossRef]
85. Koç, Ş.; Özmen, Ö.; Öksüz, N. Geochemical properties identifying the environment of manganese oxide mineralization of Kasımağa (Keskin-Kırıkkale). *Bull. Miner. Res. Explor.* **2000**, *122*, 107–118.
86. Öksüz, N. Geochemical characteristics of the Eymir (Sorgun-Yozgat) manganese deposit, Turkey. *J. Rare Earths* **2011**, *29*, 287–296. [CrossRef]

Disclaimer/Publisher's Note: The statements, opinions and data contained in all publications are solely those of the individual author(s) and contributor(s) and not of MDPI and/or the editor(s). MDPI and/or the editor(s) disclaim responsibility for any injury to people or property resulting from any ideas, methods, instructions or products referred to in the content.